Modelling tumour cell proliferation from vascular structure using tissue decomposition into avascular elements

Maximilian O. Besenhard[1,2], Monika Jarzabek[1], Alice C O'Farrell[1], John J Callanan[3], Jochen HM Prehn[1,+], Annette T. Byrne[1,4,+,*], Heinrich J. Huber[5,+,*]

[1] Centre for Systems Medicine and Department of Physiology and Medical Physics; Royal College of Surgeons in Ireland, Dublin 2, Ireland

[2] Research Centre Pharmaceutical Engineering (RCPE) GmbH, Inffeldgasse 13, 8010 Graz, Austria

[3] Department of Biomedical Sciences, Ross University School of Veterinary Medicine, St Kitts, West Indies

[4] UCD School of Biomolecular & Biomedical Science, Conway Institute, University College Dublin, Dublin 4, Ireland

[5] Department of Cardiovascular Sciences, KU Leuven, Herestraat 49, Box 911, 3000 Leuven, Belgium.

Running title: Vascular tumour proliferation studied by avascular elements

* Corresponding authors:

Heinrich J. Huber, Ph.D., Department of Cardiovascular Sciences, KU Leuven, Herestraat 49, Box 911, 3000 Leuven, Belgium. Tel + 32 1637 2099 / FAX: + 32 476 50 21 62

Annette T. Byrne, Ph.D., Centre of Systems Medicine, Department of Physiology and Medical Physics, Royal College of Surgeons in Ireland, 123 St Stephen's Green, Dublin 2, Ireland. Phone: +353 - 1 - 402 - 8673 / FAX: + 353 - 1 - 402 - 2447 / E-mail: annettebyrne@rcsi.ie

+ shared senior authorship

Abstract:

Computer models allow the mechanistically detailed study of tumour proliferation and its dependency on nutrients. However, the computational study of large vascular tumours requires detailed information on the 3-dimensional vessel network and rather high computation times due to complex geometries. This study puts forward the idea of partitioning vascularised tissue into connected avascular elements that can exchange cells and nutrients between each other. Our method is able to rapidly calculate the evolution of proliferating as well as dead and quiescent cells, and hence a proliferative index, from a given amount and distribution of vascularisation of arbitrary complexity. Applying our model, we found that a heterogeneous vessel distribution provoked a higher proliferative index, suggesting increased malignancy, and increased the amount of dead cells compared to a more static tumour environment when a homogenous vessel distribution was assumed. We subsequently demonstrated that under certain amounts of vascularisation, cell proliferation may even increase when vessel density decreases, followed by a subsequent decrease of proliferation. This effect was due to a trade-off between an increase in compensatory proliferation for replacing dead cells and a decrease of cell population due to lack of oxygen supply in lowly vascularised tumours. Findings were illustrated by an ectopic colorectal cancer mouse xenograft model. Our presented approach can be in the future applied to study the effect of cytostatic, cytotoxic and anti-angiogenic chemotherapy and is ideally suited for translational systems biology, where rapid interaction between theory and experiment is essential.

Introduction

Vascularisation of tumours is essential for their progression and, therefore, several therapeutic strategies seek to target tumour vessels [1-3]. As a consequence, studying how the structure and amount of vessel penetration give rise to differing tumour proliferation patterns is of theoretical [4, 5], diagnostic [6, 7] and therapeutic interest [8, 9]. For such studies, mathematical and computational approaches are often applied [7, 10-14]. However, most of the existing models confine themselves to the study of avascular tumour proliferation. In turn, when models consider the detailed impact of the vessel network and the resulting supply of nutrients and waste disposal, they become mathematically complex, require high computational resources and are challenged by the incorporation of complex experimental data. Hence, such models are often impractical for systems biology, where a rapid cycle of theoretical predictions and experimental findings is required to obtain new biological insight [15, 16].

A technically simple and elegant method to study the interaction of cells and their vascular environment are cellular automata [17, 18], which are often combined with differential equation approaches. As such, Patel and colleagues [19] implemented a numerically fast, partial differential equation-based approach to calculate the spatiotemporal distribution of nutrients such as oxygen, glucose and disposal of waste (lactate) dependent on the vascular supply. This approach was combined with a 2-dimensional cellular automata model to study the distribution of proliferating, quiescent and dead tumour cells and their dependence upon nutrient supply via blood vessels. However, the benefit of simplicity came at the cost of disregarding information about the vascular structure, which would require a computationally extensive 3-dimensional cellular automata approach such as the one presented by Welter [13, 14].

The aim of our study was to construct a model that includes first principle biophysical constraints on cellular migration, nutrient consumption, cell proliferation and cell death. We therefore built upon the ideas of Patel [19] and the work of the Galinsky group [11, 12]. Instead of taking into account extended complex vessel structure of an entire tumour, however, we assumed the existence and interplay of small avascular volume elements (AVEs) that make-up the tumour. Amount of vascularisation and its grade of heterogeneity can then be taken into account by different distributions of AVEs with different sizes. The AVE size distribution can then be used to calculate the number of proliferating, quiescent and dead cells in the tumour. We subsequently used the model to identify, and mechanistically explore, diverse hypotheses that relate vessel density and distribution to amount of tumour cell proliferation. We finally experimentally illustrate the presence of these novel findings by a *de novo* mouse xenograft model.

Results

A model to study vascularised tumours via decomposition into avascular elements

We pursued a pragmatic approach for studying vascular tumour proliferation that is suitable for rapid hypothesis testing. We assumed a certain vascular tumour tissue which we decomposed into avascular elements (AVEs; Fig 1A). We modelled that these AVEs exchange nutrients such as glucose, oxygen, and lactate (waste), together with cells via adjacent AVEs not separated by vessels (Fig. 1B). We reasoned that the relative AVE size distribution contains sufficient information to characterise the density and heterogeneity of tumour vascularisation (Fig 1C, having 10 different AVE sizes). For mathematical and computational simplicity, AVE's were assumed as half cylindrical volumes with height equalling their diameter and a vessel at its centre (Fig 1D). Using this decomposition, we have transformed the problem of vascular tumour proliferations to the interplay of multiple AVE of a simple geometry, allowing us to reuse modelling methods, previously applied to study avascular cell proliferation [10, 20, 21]. Following these approaches, we studied the distribution of proliferating (P), quiescent (Q) and dead (D) cells within each AVE. We were interested in the relative composition of these cells within a given tissue rather than studying absolute tumour size. This was due to the fact that we regard a high proliferative index (the amount of proliferating cells per given tissue) as a means of tumour aggressiveness, leading to metastasis and relating to a worse prognosis [22-24]. We considered changes in each tumour cell type by transition rates. These transition rates were made dependent on oxygen, glucose and lactate concentrations and amount of available space for cell proliferation (Fig 2AB, Supplementary Figure 1AB, Table 3 and methods). Exchange between AVE's was integrated by allowing a net flow of nutrients, waste and cells between AVE's of different size, accounting for inter AVE gradients. This exchange is indicated by the arrows in Fig 1B. Given that, in turn, this net flow was dependent on the actual nutrient and tumour cell concentrations of all AVEs, an iterative procedure was pursued to

solve the equations. The used workflow is shown in Fig 2C and described in detail in the method section. The entire procedure was repeated for each tissue with a given vasculature.

Calculation of an exemplary AVE size distribution from a virtual tissue as model input

The relative AVE size distribution is the model's starting point. Such AVE size distribution can be obtained from 2D and 3D images of entire tissues by any classical tiling approach [18, 25, 26]. For our subsequent calculations, we however opted for a simpler procedure. The detailed procedure is described in the methods and was used for the entire calculations. We thereby generated an artificial 2D tissue. In this tissue, we distributed points that represent vessel, assuming inter vessel distances (IVD) that were taken from histology of colorectal carcinomas [27]. We subsequently used an algorithm to calculate the distance for each point of this artificial tissue to the nearest vessel, giving us a histogram for AVE sizes. We specifically assumed an average inter vessel distance of 75 μM, but with different heterogeneity in vascular structure (Fig 3AB). In the remainder of the manuscript we will refer to them as homogeneous and heterogeneous vasculature (Fig 3C, red and black bars).

The model predicts increased cell proliferation and death upon higher vessel heterogeneity

Having determined a distribution of AVE sizes that represent a homogenously and heterogeneously vascularised tissue with the same average IVD (Fig 3C), we then investigated the effect of the different amount of vascularisation on the distribution of proliferating, quiescent and dead cells. We found that, while a homogenous tissue leads to very little proliferation and only limited cell death, a heterogeneous distribution led to 12% cell death and 10% proliferating cells (Fig 3D). To investigate this further, we looked at the distribution of P, Q, and D cells in AVEs of different types. In the homogenous tissue, we observed some cell

death in the larger AVEs 6-10 (Fig 3E), but this effect was greatly diminished once weighting over the volume distributions for AVES of the entire tissue (Fig 3F; bars equal to 100%). In contrast, looking at AVEs of a heterogeneous tissue, we found markedly more proliferation in the smallest AVE and more cell death in the larger ones (Fig 3G), such that the effect of proliferation and death was preserved when the contribution of each AVEs to the entire tissue was assessed (Fig 3H). Moreover, a small effect of proliferative compensation, whereby dead cells are replaced by nascent cells was observed in larger AVEs (small black area in Fig 3G) and also contributed slightly to the overall higher rate of proliferating cells in a heterogeneous tissue (Fig 3H). We conclude that a higher heterogeneous tissue leads to spatial areas with high cell proliferation and high cell death as a consequence of having rather small and rather large AVEs. In contrast, a homogenous tissue led to a high amount of quiescent cells due to a modest distribution of AVE sizes causing no significant compensatory proliferation of dead cells (see illustration in Supplementary Figure 1CD).

Sensitivity analysis suggests stability of our model to AVE partition

Due to the higher proliferation characteristics of the heterogeneous tissue, suggesting higher tumour aggressiveness, we focussed on this in the further analysis. As certain parameters had to be estimated in the model, we wanted to consider their influence on the cellular composition. We therefore increased or decreased each of these 12 parameter by 10% and calculated absolute changes in relative or absolute cell compositions (see Fig 4AB and Supplementary Figure 2AB, respectively). This sensitivity analysis revealed that vessel permeability (ϑ), oxygen consumption (f_{o_Q}) and the proliferation threshold for oxygen ($c_{o\ PT}$) were fairly influential factors. In addition, the robustness of the model was tested by increasing the number of AVEs, therefore representing finer grained AVE size distribution. This yielded a slight decrease of absolute cell numbers compared to the unchanged model (Supplementary Fig 2C), but,

otherwise, lead to almost the same cell compositions when the number of AVEs was increased (Fig. 4C).

Model calculation for different IVDs suggests that cell proliferation may increase when vascularisation decreases

We next investigated the change of cell composition for different vessel densities. We therefore repeated our calculation of the AVE distribution from a virtual tissue using the method described before (Fig 3AB) and using a different average IVD as basis. As expected, calculating the amount of proliferating, quiescent and dead cells, we found that that the amount of total cells decreased with decreased vessel density (increased IVD), suggesting that under a very low vessel density, the tumour cannot sustain a large number of cells (Fig 5A). This decrease was matched by a decrease of quiescent cells. However, when analysing the amount of proliferating and dead cells, we found that their amounts were increasing with increasing IVD until a peak was reached around an average IVD~80, followed by a subsequent decrease at higher IVDs. Looking at the predicted oxygen and glucose levels (Fig 5BC), this surprising results could be explained by a trade-off between two effects. Firstly, at low IVDs, tissue nutrient perfusion was high, and hence amount of cell death and compensatory proliferation was low. When tissue becomes less vascularised, cells started to die, while enough supply was available to allow for compensatory proliferation. At higher IVD, however, oxygen levels fell under the threshold that is necessary for cell proliferation (Fig 5B small dashed line), leading to decreased proliferation and contributing to a further decrease in overall cell numbers. However, oxygen levels remained high enough to sustain cellular survival (Fig 5B, dotted line) and therefore cell death continued to decrease as consequence of the decrease in total amount of cells. Finally, cellular glucose levels dropped while lactate levels increased when the average IVD was increased (Fig 5CD). All entities, oxygen, glucose and lactate, eventually reached a

constant value. This constant value was established since not only nutrient perfusion of the tissue, but also nutrient consumption (due to a lower amount of cells) decreased when IVD increased. We further note that the calculated oxygen and glucose levels were consistent with physiological values [28-30] and experimental data of 0.08 mM and 5.5 mM as determined by [31]. In addition, we remark that values of oxygen, glucose and lactate at low vessel densities are consistent with those for mild hyperglycaemia, acidosis and hypoxia which are likely conditions in less perfused regions of the outer tumour rim.

We then investigated the amount of proliferation and cell death in regions close to the proliferation peak. We therefore selected two average IVD values, IVD = 64 and IVD= 85 and re-used the method of Fig 3AB to calculate vessel distributions associated to each IVD. We then calculated the amount of proliferating and dead cells. We observed an increase in cell proliferation of 38% and cell death of 31% (Fig 5E) when the average IVD was increased from 64 to 85. Analysing the relative contribution from each AVE between both distributions, we found that the increased proliferation was observed mainly in the smallest AVE. In contrast, the amount of dead cells was found in medium and larger AVE, together with a small concomitant increase in compensatory proliferation (Fig 5FG). We note that the assumption of a 37% increase in the average IVD between IVD = 64 and IVD= 85 (which is around the published value of IVD =75) [27] will be useful in the subsequent experimental analysis.

Decrease of micro vessel density is linked to increased tumour proliferation in subcutaneous HCT116-luc2 tumour

Our modelling results provided evidence that an increased proliferation can be present even under decreased vascularisation (i.e. increased IVD) within certain vascularisation regimes. We therefore were interested if we could illustrate this relation by an experimental case. To do

so, we required a model system for rapid hypothesis testing where the same type of tumour was analyses under a different amount of vascularisation. We hence used a mouse xenograft model established in our laboratory [32] where human HCT116-luc2 colon cancer cell lines were subcutaneously (SubQ) implanted into Balb/c nude mice. We sacrificed mice at day 8 (n = 2) and day 18 (n = 2) post-implantation and analysed tumours histologically in 10 independent fields of the outer tumour rim from 2 mice at each time point.

We first used IHC staining with PECAM1/CD31 antibody to determine the microvessel density (MVD) which is an experimental measure of the level of vascularisation and which has an inverse relationship to the IVD we used in the model. We observed a significant ($p = 0.006$) decrease in MVD of about 27 % from 22.4 ± 2.4 (day 8) to 16.3 ± 2.0 (day 18) (Fig. 6 A-C). The observed decrease in MVD in our SubQ model may be the result of increased biomechanical forces and vessel instability from day 8 to 18 as suggested by theoretical studies [33]. However, we were not interested in rigorously further pursuing this effect, but aimed to check the emergent consequence of this MVD decrease on the amount of proliferating and necrotic cells. We note that this decrease in MVD of 27% between day 8 and day 18 translates to an increase of IVD of 37% such as the one from IVD=64 (day 8) to IVD=85 (day 18) as assumed by Fig 5.

We therefore repeated the analysis on the same tumours using KI67 staining for proliferating cells and TUNEL staining of cells dead by apoptosis, which is the predominant type of cell death in the outer rim region. Interestingly, despite decreased MVD, we identified a significant ($p = 0.0006$) increase in cell proliferation from 19.7 ± 1.7 % (day 8) to 28.3 ± 1.6 % (day 18) (Fig 6 D-F). This 44% increase in proliferation was a bit higher than model predictions of increased proliferation of 38% that was calculated from our model when IVD was increased from IVD=64 to IVD=85. Likewise, TUNEL apoptosis staining from ten independent fields of the same tumours revealed a non-significant ($p = 0.098$) increase of number of TUNEL-

positive cells per field of view from 5.8 ± 0.7 (day 8) to 8.0 ± 0.8 (day 18), reflecting an 38% increase that coincides with a model prediction of a 31% increase (Fig. 6 G-I).

Discussion

In this study, we developed a method to investigate how complexity and amount of vessel structures is correlated with tumour cell proliferation and death within a tissue. The benefit of this approach lies in its easy integration of experimental data, numerical speed and in the fact that neither large scale geometric information nor sophisticated numerical calculations are needed, allowing for a rapid cycle between theoretical predictions and preclinical validations.

The input to our approach are size distributions of avascular elements (AVE's) that give abstract information about vessel density and grade of heterogeneity at certain time points of the tumour. We wish to highlight here that our approach is therefore independent of the way these distributions are calculated. Here, we generated an AVE size distribution by applying a simple tiling method using stochastic seeding of test points and investigated the distance to the nearest vessels. For this specific method we assumed vessel distribution along a simulated 2D tissue. Hence, we did not take into account physiological branching structures, whereby larger vessels branch successively into smaller ones in a tree-like fashion to guarantee optimal nutrient support [34]. Therefore, any method to calculate AVE size distributions from realistic vascular tumours would require more sophisticated approaches in a 3D space [25, 26] such as Voronoi tessellation [18]. Nevertheless, such a physiologically homogenous vessel branching would also be expected to have a lower dispersion of AVE volume sizes than a heterogeneous one [35], exactly such as in our approach.

The developed model predicts that tumours with a heterogeneous vessel distribution exhibit higher proliferation and more cell death compared to tumours with equal vessel densities and a more homogeneous vessel distribution. This is due to a higher spread of the AVE size distribution for tissues with higher heterogeneity resulting in areas with a high nutrient supply, and thus greater proliferation, but also areas with low nutrient supply and cell death. Our

predictions are consistent with experimental findings from mouse mammary xenografts where tumour cell proliferation was mainly observed close to areas surrounded by vessels [36]. Because of their higher cell turnover (more cell death and consequent higher compensatory proliferation), tumours of heterogeneous tissues may thus have higher mutation rates, better genetic adaptation and higher aggressiveness. It is therefore tempting to speculate that by reducing heterogeneity as done by VEGF-inhibitors such as Avastin, mutational rates may be lowered in highly heterogeneously vascularised tumours and, hence, malignancy may be mitigated or tumours may be more amenable to standard treatments [37-39].

Using the gold-standard HCT-116-SQ mouse xenograft, we have observed a decrease in MVD of tumours in the colorectal cancer model employed. While this result warrants a more rigorous investigation, a similar finding has been observed previously by Hemmerlein 2001 et al [40]. It was, however, not our aim to investigate vascularisation kinetics during tumour growth or even compare our mouse model to others, as this would have required a larger scale investigation. For our approach this change in MVD was a convenient choice to study the effects of changed microvessel density on the cell proliferation in a tumour.

Our modelling approach qualitatively reflected the trend of our mouse model that vessel density negatively correlates with tumour proliferation under some regimes of vascularisation. The effect was explained by a trade-off between increase in compensatory proliferation for replacing dead cells and a decrease of cell population due to lack of oxygen when nutrient perfusion gets low. Our combined model and experimental efforts therefore suggest that the apparently trivial relationship between increased vascularisation and proliferation does not necessarily hold for all situations. Consistent with our findings, Lee and co-workers found an inverse correlation between microvessel density and numbers of apoptotic cells in mammary

ductal carcinoma. They further reported an inconclusive relationship between microvessel density and proliferation [9], disputing the notion that vascularisation is intrinsically linked to higher proliferation in all vascularisation regimens. Besides these qualitative predictions, we predicted quantitative changes of oxygen, glucose and lactate during changes of the IVD which can be validated in follow-on experimental studies. Specifically, we note that our values of 50-150 nmol/cm^3 oxygen (0.05-0.15 mM), 3-4.5 μmol/cm^3 glucose (3-4.5 mM) and 1-2.4 μmol/cm^3 (1-2.4 mM) of lactate are in excellent agreement with physiological levels of glucose 2-5 mM and lactate (0.5-2.2 mM; [28]) in blood and with oxygen and glucose levels from Jiang *et al* [31] of 0.08 mM and 5.5 mM.

The validity of our model is confined to studying the proliferation characteristics in the outer rim of the tumour. Specifically, we neglected the necrotic core which is the most decisive factor for tumour expansion. Taking into account the necrotic core would have resulted in discontinuous AVE size distribution with the necrotic core as one large AVE that is connected to several smaller ones. This would have violated our assumption that all AVEs are continuously distributed and connected with each other in an equal manner. Moreover, the high space demand in the tumour core would require us to take into considerations high biomechanical forces which would be at odds with our model of free nutrient diffusion and the simple convective-diffusive transport of cells (Equations 4-5). Therefore, instead on focussing on tumour expansion, we rather investigated the proliferative index of a given tissue. Indeed, the KI67 proliferative index is positively correlating with tumour grade, metastasis and worse prognosis in solid tumours [22-24], rendering the fact that cancer dead is more related to the propensity of metastasis than with growth of the primary tumour [41, 42]. Likewise, Vartian and Weidner observed that KI67 staining in the tumour cores of samples from patients with

breast carcinomas was 45-fold greater than in adjacent tissue [7], demonstrating the relevance of this parameter for tumour progression

Other models have been developed to study the effects of vascularisation using cellular automata [13, 19, 43, 44], stochastic differential equations [45] or multiphase model approaches [46, 47]. Even if they were experimentally validated, such models are often restricted to the study of tumour spheroids and not applied to the study of vascularised tumours [10, 21]. Indeed, approaches using cellular automata easily become computationally complex and cannot be applied for studying larger tumours. In contrast, our presented model can be studied with the same mathematical and numerical formalism for tumours of different sizes. As our tiling method for studying AVEs may require finer granularity for larger and more heavily vascularised tumours, restrictions in tumour size may only apply indirectly. Nevertheless, the computational effort of our algorithm scales with linear power in the number of different vascular elements N for the equations 1-3 and has only quadratic dependency on the amount in the exchange term equation 4-9, which for the current calculation consumed less than 10 % of calculation time. This may become prominent for higher values of numbers of AVEs. In contrast, Cellular Automata approaches scale with the cubic power of the number of grids used per tumour length. This together with the smaller numbers of AVEs compared to the amount of grids gives our approach an advantage over 2D and especially 3D Cellular Automata approaches with respect to numerical costs.

In conclusion, the model concededly has its limitations. Firstly, as the model cannot account for studying growth of the necrotic core, it cannot be used to assess the size of the tumour, but focuses rather on studying a proliferative index dependent on amount and type of vascularisation. Secondly, we modelled only tumour cells and not tumour stromal cells. Hence,

the formalism shall be adapted when other regions than the proliferative tumour rim are modelled such as adjacent adipose tissue which would have other metabolic and proliferative rates. We further only provided a qualitative estimation of cell and nutrient exchange terms (Eq. 4 and 5) and this formalisms may be further improved once a theory of convection and diffusion of cells and nutrients is available. We finally mostly refrained from going into predictions on a too quantitative level. We rather used the model as a tool to assess potential relevant qualitative effects that arise during tumour proliferation as consequence of different amounts and different heterogeneity of vascularisation. Indeed, we are not entirely sure that all parameters to remodel a quantitative proliferative response are experimentally known and controlled, and hence only focussed on those experimental parameters that are currently widely accepted to control tumour proliferation. Despite these drawbacks, we provide here a pragmatic model that includes first principle biophysical constraints. With this concept, we were able to tackle the complex problem of vascular tumour proliferation by decomposing the tissue into avascular elements, allowing us to reuse concepts from modelling spheroids. We preferred this first-principle, qualitative approach over a merely fitting exercise where parameters are adapted to correct for the inevitable model abstractions of a highly simplified model. We demonstrated that this model concept can serve as a template for analysis of experimental tumour models and that it was even possible to render trends of cell proliferation and cell death under altered vasculature. We present this approach to the readers of JTB for further elaboration by the biophysical community in follow on studies. In the future, our approach can be extended to integrate mechanisms of tumour vessel development [25, 26] or to include the effect of cytotoxic and cytostatic chemotherapy, which could be simply implemented by making the cell transition rates of Fig. 2B dependent on drug action. Likewise, it would allow the study of anti-angiogenic drugs by modelling their impact on tumour vasculature and exploiting the model to assess changes in tumour cell composition.

Methods

Ethics statements

All animal experiments were performed by licensed investigators in accordance with animal research guidelines (Department of Health and Children, Dublin, Ireland) and protocols were approved by the Animal Research Ethics Committee at University College Dublin, where the work was performed. Animals were housed in groups, maintained on a 12 hour light/dark cycle, with access to food and water ad libitum.

Modelling vascularised tumours by decomposition into avascular elements

A semi-phenomenological approach was chosen to account for the influence of the vascular system. Thereby, the vascular system was assumed to serve as source and drain for nutrient and waste and thereby affect tumour proliferation [11]. To facilitate calculation of nutrient supply and waste removal, the complex 3-dimensional vessel structures was replaced assuming the tissue to be composed of avascular elements (AVEs). An illustration of the concept is given in Fig. 1A-B. AVE volumes with the characteristic radius R_{AVE} and their relative fractions were estimated by the following procedure. AVEs were assumed to have a geometry that is simplified to half cylinders whose height equalled their diameter. A vessel with a constant radius was assumed to be located at the cylinder's centre (Fig 1D). Due to this approximation cylindrical coordinates and periodic boundary condition (Table 5) could be used, allowing for a simplified (i.e., one dimensional) calculation of nutrient and cell profiles within the AVE volume. The relative fraction of AVEs of different sizes, (i.e., the AVE size distribution), represents the underlying vessel structure such as vessel density and regularity. The AVEs were assumed to be connected with each other to allow the exchange of cells, nutrients, and waste. Mathematically, this exchange was incorporated with the aid of the exchange source terms in the PDEs as described below. Boundary conditions according to Table 4 were assumed to

model transport of nutrients/waste out of/into blood vessels. The transport dynamics was made dependent on the concentration gradient at the vessel wall and its selective permeability as in [19]. Migration of cells between the vessel and the tumour was disregarded.

Quantification of relative occurrence of avascular elements

To obtain an AVE size distribution from intervessel distances (IVD), we created a 2D virtual tissue whereby we spotted virtual vessels with the given IVD (=75 μm) and with a vessel diameter ($r_{vessel} = 1.94$ μm) that reflected previously published data (Fig. 3AB) [27]. To generate homogeneously and heterogeneously virtual tissues of the same vessel density, spots (representing the vessels) were equidistantly distributed for both tissue types. In the case of the heterogeneous tissue, twice as many spots were placed initially and half of them were removed arbitrarily to create an irregular pattern. In order to obtain the AVE size distribution that represents a tissue, 10 000 test points were randomly placed into the virtual tissues. Afterwards, distance distributions of these points from the two nearest vessels were determined (r_{v1}, r_{v2}), and the characteristic length of an AVE was defined by $R_{AVE} = ½ \cdot (r_{v1} + r_{v2})$. AVEs were binned into 10 equally spaced containers according their characteristic radii R_{AVE} ($R_{AVE} = [R_{AVE\,min}, \dots, R_{AVE\,i}, \dots, R_{AVE\,max}]$; $R_{AVE\,min}$ = 76 μm, $R_{AVE\,max}$ = 103 μm for homogenous and $R_{AVE\,min}$ = 61 μm, $R_{AVE\,max}$ = 204 μm for heterogeneous tissue) leading to a histogram of relative occurrence ω_i, hist $R_{AVE} := \boldsymbol{\omega} = [\omega_1, \dots, \omega_i, \dots, \omega_{10}]$.

Finally, to account for the fact that randomly placed points have a greater likelihood to be counted by this procedure due to their larger area [48], the probability distribution of the recorded histogram $\omega(\mathrm{X}_\omega)$ was weighted by the AVE cross section $\mathbf{A}_{\boldsymbol{\omega}} = [\mathrm{A}_{\min}, \dots, \mathrm{A}_\mathrm{i}, \dots, \mathrm{A}_{\max}]$ with $\mathrm{A}_\mathrm{i} = {R_{AVE\,i}}^2 + {r_{vessel}}^2$. The relative occurrence of AVEs in the tissue $\boldsymbol{\omega}(\mathrm{R}_{\mathrm{AVE}})$ is plotted in Fig 3C, whereby homogenously and heterogeneously vessel

distribution differed in the spread of the covered range of characteristic radii. From the characteristic radii, AVE volumes were created according to the formula of half cylinders with same height as diameter $Vol_i = \pi \cdot (R_{AVE\,i}{}^2 - r_{vessel}{}^2) \cdot 2 \cdot R_{AVE}$. The volume distribution is hence characterised by those from the corresponding radii with an x-axis that scales with the third order of the radii.

As mentioned above the vessel homogeneity in this paper denotes an average distribution of vessels in two dimensions, and not a physiologically observed 3-dimensional tree-based vessel structure.

Dynamic equations of oxygen, glucose, waste and tumour cell types within AVEs

To calculate the dynamics of nutrients, waste and tumour cells within a particular AVE, a framework as frequently applied to tumour spheroids was followed. Therefore, tumour proliferation profiles within each AVE were calculated by determining spatiotemporal profiles of different tumour cell types. Consistent with approaches in [49, 50] the number of proliferating (P), quiescent (Q) and dead (D) cells (as a collective term for all types of cell death) per volume unit was assumed. Their evolution was influenced and in turn influences the availability of glucose (g), oxygen (o) and waste (w, lactate within this work).

Oxygen, glucose, and waste were assumed to penetrate via the vessels walls. While oxygen and glucose are consumed, waste is produced by proliferating or quiescent tumour cells (P, Q). The temporal (time t) and spatial (radius of the AVE r) evolution of their concentration c_o (r,t), c_g (r,t) and c_w (r,t) within each AVE is given by the following-reaction diffusion equations:

$$\frac{\partial c_o}{\partial t} = \nabla \cdot (D_o \cdot \nabla c_o) + f_o(P, Q, N)$$

$$\frac{\partial c_g}{\partial t} = \nabla \cdot \left(D_g \cdot \nabla c_g\right) + f_g(P, Q, N)$$
$$\frac{\partial c_w}{\partial t} = \nabla \cdot (D_w \cdot \nabla c_w) + f_w(P, Q, N) \qquad \text{Equation 1}$$

In the partial differential equations (PDEs) in Equation 1 the first term on the right hand side describes the diffusion of oxygen, glucose and waste with respective diffusion constants D_O, D_G, D_W, assuming that these entities diffuse homogenously through the entire tissue. The entities f_o, f_g, f_w denote the source terms that account for change of oxygen, glucose or waste by their turnover (consumption or production) and the diffusive exchange of oxygen, glucose or waste among AVEs (via exchange terms as described later).

The source terms of Eq. 1 were modelled by

$$f_o = P\, f_{o_P} + Q\, f_{o_Q} + AVE_{ex\,o}$$
$$f_g = P\, f_{g_P} + Q\, f_{g_Q} + AVE_{ex\,g}$$
$$f_w = P\, f_{w_P} + Q\, f_{w_Q} + AVE_{ex\,w} \qquad \text{Equation 2}$$

whereby oxygen and glucose were consumed by proliferating P (with rate per cell of f_{o_P} and f_{g_P},, respectively; Table 1) and quiescent cells Q (with rate per cell of f_{o_Q} and f_{g_Q}; Table 1). Likewise, f_{w_P} and f_{w_Q} were the rate of waste production by proliferating and quiescent cells, respectively. The terms $AVE_{ex\,o}$, $AVE_{ex\,g}$, $AVE_{ex\,w}$ were denoted in this paper as AVE exchange source terms and account for the exchange between AVEs of different size as subsequently described.

The spatiotemporal concentration of all cell types (P(r,t), Q(r,t), D(r,t)) was modelled by

$$\frac{\partial P}{\partial t} = \nabla \cdot (D_P\, \nabla P) + K_B\, P - K_Q(c)\, P + K_P(c)\, Q + AVE_{ex\,P}$$
$$\frac{\partial Q}{\partial t} = \nabla \cdot \left(D_Q\, \nabla Q\right) + K_Q(c)\, P - K_P(c)\, Q - K_D(c)\, Q + AVE_{ex\,Q}$$

$$\frac{\partial D}{\partial t} = \nabla \cdot (D_N \nabla D) + K_D(c)\, Q - K_R\, D + AVE_{ex\,D} \qquad \text{Equation 3}$$

with c denoting the dependency of above parameters on oxygen, glucose and waste concentration as described below. As before, all cell types were modelled to diffuse within the extracellular matrix as given in the first term on the right hand side of each equation and characterised by the effective diffusion constants D_p, D_q and D_d. These diffusion constants were modelled to depend on the total cell density ($cd = P + Q + D$) to account for diffusion impairment due to increased cell crowding following the approach of Gatenby [11, 12]. Here, the density-dependent effective diffusion coefficients were defined as $D_P = D_p\, a,\ D_Q = D_q\, a,\ D_D = D_d\, a\ D_P = D_p\, a,\ D_Q = D_q\, a,\ D_D = D_d\, a$. We thereby set $a = \exp(\frac{-5\ cd}{cd_{max}})\ cd_{max}$ to obtain a stable decaying function with cell density cd and used the constant 5 to have diffusion sufficiently blocked at maximum cell densities cd_{max} (<1% of max).

Further terms at the right hand side of Equation 3 characterise the transition of cells between of different types (P, Q, D) as illustrated in Fig. 3A. For these terms in Equation 3 the transition parameter K_B denotes the rate of cell birth, K_Q the rate at which proliferating cells become quiescent, K_P the rate at which quiescent cells become proliferating, K_D the rate of quiescent cells dead and K_R accounts for the disintegration and removal of dead cells which was assumed to be $K_R = K_r \cdot \exp(-100 \cdot R_{AVE})$. The factor 100 cm^{-1} was assumed to allow for a moderate dependency with AVE size (as R_{AVE} was given in cm for our calculations, therefore the exponential factor varied around 1 for a typical AVE). The factor K_r (Table 1) was assumed to reflect a half time of degradation of 1.5 h which was considered as the typical time for phagocyting dead cells. K_P, K_Q, and K_D are described below. K_B, was constant while K_R was made dependent on the AVE size to account for slower removal rates and response times (e.g. due to macrophages clearing the cellular debris) in the case of bigger AVEs.

Transition rates between tumour cells and their dependency on nutrients, waste and cell density

According to a procedure as given in [49, 50], tumour cells of different kinds were assumed to change their state as given in Fig 2. The respective transition rates for cell proliferation K_P, for proliferating cells becoming quiescent K_Q and for quiescent cells to die K_D were modelled to be dependent on the cell density, and the concentration of oxygen, glucose and waste. Three different types of thresholds for oxygen, glucose and waste levels were introduced to incorporate the combinatorial effect of different nutrient/waste concentrations (see Table 1) on cell transition. These were the survival thresholds ($c_{o_T}, c_{g_T}, c_{w_T}$), proliferation thresholds ($c_{o_{PT}}, c_{g_{PT}}, c_{w_{PT}}$) and a threshold for optimal conditions ($c_{o_{opt}}, c_{g_{opt}}, c_{w_{opt}}$). For the making the transition rates dependent on nutrient and waste distribution (i.e., c_o, c_g and c_w), three specific conditions, denoted here as limit conditions, were assumed as follows:

Rates under condition of cell death: Whenever either oxygen or glucose supply was assumed to fall below ($c_o < c_{o_T}$; $c_g < c_{g_T}$), or waste was to exceed ($c_w > c_{w_T}$), the respective survival thresholds, proliferating cells were assumed to become quiescent and quiescent cells were assumed to die ($\mathrm{K_P} = 0,\ \mathrm{K_Q} > 0, \mathrm{K_D} > 0$). The following rules for transition rates at the different thresholds apply:

Rates at the proliferation threshold: Whenever oxygen and glucose were exceeding the respective proliferation thresholds ($c_o > c_{o_{PT}}$; $c_g > c_{g_{PT}}$), and the waste level was undergoing the latter ($c_w < c_{w_{PT}}$), quiescent cells were modelled to become proliferating ($K_P > 0$) and the rate of cell death was assumed to be zero ($K_D = 0$).

Rates at and above the threshold for optimal proliferation: When, at the same time, oxygen and glucose concentration were above and waste concentration below the threshold for optimal conditions ($c_o \geq c_{o_{opt}}$, $c_g \geq c_{g_{opt}}$, $c_w \leq c_{w_{opt}}$), proliferation was maximum and rates for cells becoming quiescent or dead were zero ($K_P = K_p$, $K_Q = 0$, $K_D = 0$).

These limit conditions for cell transition rates are summarized in Table 2. Values for K_P, K_Q, K_D between these limit conditions were interpolated via steady, differentiable, and monotonous functions of these transition rates for the entire range of glucose, oxygen and waste concentration. Therefore, cosine and sine functions scaled to the descending and ascending quadrant were chosen to have everywhere differentiable function that reflect the monotonous dependency of transition rates on the concentrations of nutrients and lactates (Table 3). Supplementary Figure 1AB depict how K_P and K_Q depend on oxygen and glucose.

Furthermore, we assumed cell transition rates to be dependent on the cell density. Cell proliferation was only possible if the cell density cd was below the maximum density $cd_{max} = 5 \cdot 10^8$ [cells/cm^3] according to [12]. This value is in good agreement with those obtained for EMT6/Ro tumour spheroids ($cd = 3 - 5 \cdot 10^8$ [cells/cm^3]; [51]). To avoid that continuous cell proliferation could lead to cell densities higher than maximum value cd_{max}, the transition rate K_P was made to decrease and K_Q to increase with increasing cell densities ($cd \rightarrow cd_{max}$) as described in Table 4. Likewise, the factor in K_Q in Table 4 was chosen to restrict the total amount of cells to cd_{max}.

Calculation of the AVE exchange source terms AVE_{ex}

AVE's of different sizes were assumed to be connected to each other (and are not fully separated by the vessel network). Therefore, cells, nutrients and waste were assumed to exchange among AVE's of different volumes. Consequently, disequilibrium in cells, nutrients

and waste results in a net flow of the latter between adjacent AVEs. We assumed that all AVEs were connected equally with each other, according to their relative occurrence $\boldsymbol{\omega}(\mathrm{R_{AVE}})$. This net flow was introduced in Equation 2-3 and denoted as exchange source terms AVE_{ex}.

Within the following we describe how the exchange source terms for oxygen and for proliferating cells ($AVE_{ex\,o}$ and $AVE_{ex\,P}$, respectively) were calculated at each iteration step, assuming above average nutrient, waste or cell concentrations to be known. Calculations of source term corrections for glucose $\left(AVE_{ex\,g}\right)$ and waste ($AVE_{ex\,w}$) and other cell types ($AVE_{ex\,Q}$, $AVE_{ex\,D}$) follow the same scheme. These exchange terms were assumed to be spatially independent. Therefore, the $\mathrm{AVE_{ex}}$ terms could be considered to be constant over the entire distance of exchange which is the sum of the characteristic length $\mathrm{R_{AVE_i}}, \mathrm{R_{AVE_j}}$ of adjacent AVEs.

We first determine transfer rates for dissolved species such as nutrients and waste between AVE_i and AVE_j. We note that this exemplary choice of two AVEs does not require any specific spatial arrangements or other constraints, besides being of different size.

As example we calculated the oxygen exchange rate $ave_{ex\,o}$ which was assumed to be dependent on the gradient between the average concentrations in the AVE ($c_{o\,AVE_i}$, $c_{o\,AVE_j}$) as

$$ave_{ex\,o} = D_o \cdot \frac{c_{o\,AVE_i} - c_{o\,AVE_j}}{\left(R_{AVE\,i} + R_{AVE\,j}\right)^2}. \qquad \text{Equation 4}$$

Equation 4 describes diffusive transport which is based on a flux rate according to Fick's law of diffusion. The law assumes particles to move through a virtual area perpendicular to the diffusion direction and, hence, this flux is inversely proportional to the area spanned by the radii of both AVEs ([52], Supplementary Text 1).

In contrast to nutrients and waste where diffusion is quick and dominates the transfer, the calculation of cellular transfer rates such as proliferating cells ($ave_{ex\,P}$) has also to account for convective transport. This convection is driven by different cellular occupancies leading to differential space restrictions and consequent pressure equilibration between AVEs. This generates a diffusion independent convective net flow that is dependent on the difference of cell densities in each AVEs ($cd_{\,AVE_i}$), but independent of the actual cell type (i.e. not driven by entropy). Consequently, we combined the diffusion term, here shown for proliferating cells, with a convective term (on the right side of Eq. 5)

$$ave_{ex\,P} = D_p \cdot \frac{P_{\,AVE_i} - P_{\,AVE_j}}{(R_{AVE_i} + R_{AVE_j})^2} + \frac{10^4}{cd_{max}} \cdot \frac{cd_{\,AVE_i} - cd_{\,AVE_j}}{(R_{AVE_i} + R_{AVE_j})^2} \quad . \qquad \text{Equation 5}$$

We note that this represents a net flux that is analogous to the one of a convection-diffusion equation [53]. Thereby, the factor ($\frac{10^4}{cd_{max}}$) of the second, convective term was adjusted to render cell occupancies for all AVEs which were assumed to vary only within a reasonable range of 20% between the smallest ($Vol_{AVE\,min}$) and biggest ($Vol_{AVE\,max}$) AVE. We note that this term presents solely a heuristic expression for convective transport that is consistent with above biological assumptions as no current detailed theory of cell convection within tumours is available.

Above transfer rates were subsequently used to calculate the temporal change (exemplified here for oxygen) in AVE i and j by weighting the exchange among AVEs according to their volumes to guarantee conservation of mass (i.e. cells or species)

$$\frac{\partial c_{o\,AVE_i}}{\partial t} = -\,ave_{ex} \cdot \left(\frac{Vol_{AVE\,j}}{Vol_{AVE\,j} + Vol_{AVE\,i}} + 0.5 \right) \qquad \text{Equation 6}$$

$$\frac{\partial c_{o\,AVE_j}}{\partial t} = +\,ave_{ex} \cdot \left(\frac{Vol_{AVE\,i}}{Vol_{AVE\,j} + Vol_{AVE\,i}} + 0.5 \right) .$$

By solving Equation 6, the net flow rates (here for oxygen) between two AVEs during a time step Δt can be determined as:

$$c_{o\ AVE_{i,j\to AVE_{j,i}}} = \frac{(c_{o\ AVE_{i,j-start}} - c_{o\ AVE_{i,j-end}})}{\Delta t}, \quad \text{Equation 7}$$

whereby $c_{o\ AVE_{i,j-start}}$ and $c_{o\ AVE_{i,j-end}}$ denote the oxygen concentrations at the beginning and end of a time step. Then, to capture the oxygen exchange between all AVE's during a time step, we define the matrix

$$\boldsymbol{M}_{\boldsymbol{c_{o\ AVE}}}(i,j) = \begin{bmatrix} c_{o\ AVE_1\to AVE_1} = 0 & \cdots & c_{o\ AVE_j\to AVE_1} \\ \vdots & \ddots & \vdots \\ c_{o\ AVE_1\to AVE_j} & \cdots & c_{o\ AVE_i\to AVE_{j=i}} = 0 \end{bmatrix}. \quad \text{Equation 8}$$

We further assumed that all AVEs are equally connected with each other. This assumption requires that AVE distributions are continuous (i.e. no single large AVE such a necrotic core). It further requires that the AVEs in any heterogeneous distribution would be rather statistically distributed within the tissue, while for homogenous distribution (having smaller differences of AVE sizes) the exchange term would have minor impact.

Finally, the exchange source term of an AVE i (here for oxygen) was obtained by summing up the exchange with all AVE's during a time step, weighted by the relative AVE occurrence ω_i ($\sum_i \omega_i = 1$):

$$AVE_{ex\ o} = \sum_{j=1}^{N} \omega_j \cdot \boldsymbol{M}_{\boldsymbol{c_{o\ AVE}}}(i,j), \quad \text{Equation 9}$$

Solution and numerical procedure for calculating proliferating, quiescent and death cells considering inter-AVE exchange

The differential equations 1-3 that describe spatiotemporal cell distributions within the AVEs and the equations 4-9 that describe the exchange terms between AVEs form a self-consistent problem. This means that from spatial distributions of nutrients, waste and P, Q and D cells in each AVE (as calculated via Eq. 1-3), the AVE exchange terms have to be calculated according to Eq. 4-9. In turn, the exchange terms feed again into the differential equation 1-3, requiring the need for an iterative procedure.

The iteration was performed for a small, but finite time interval ($\Delta t = 1$ h), for which we could assume the AVE exchange terms as constant. This assumption of constant AVE exchange terms allowed to decouple equation 1-3 from equation 4-9 in their time dependency, facilitating the numerical solution. The iteration at a certain time step was continued till AVE exchange terms converged. After convergence of AVE exchange terms, the iteration was started again for the successive time step of the same finite time interval, $\Delta t = 1$ h. Therefore, AVE exchange terms can change for successive time steps, but remain constant during each time interval. The exchange source terms of the first iteration were initialised using the values of the previous time interval. The workflow of this nested iterative procedure was shown in fig. 2C. This procedure was repeated until cell densities of P, Q and D cells did not change (<< 0.1%) during subsequent time intervals. Usually this was reached after 400 time steps and was greatly independent of initial conditions (used for the first time interval; see supplementary Figure 3).

We note that above time intervals have a specific biological interpretation within the framework of the described numerical procedure. The reason is that the procedure assumes that a certain vasculature is present and that cell compositions and their spatial distributions adapt over time starting from arbitrary initial conditions. After this adaption, time intervals refer to the speed of how cell compositions evolve in response to a change in vasculature (a disequilibrium that is given between the actual and the optimal spatiotemporal cell composition).

Finally, concentration for proliferating (P), quiescent (Q) and dead cells (D) for the entire tissue were obtained by weighting the P, Q, N numbers of each AVE by the relative occurrence of the AVE and multiplying by its volume, e.g. $P = \sum_i P_{AVE\,i} \cdot \frac{Vol_i \cdot \omega_i}{\sum Vol_i \cdot \omega_i}$. All calculations were performed using MATLAB R2014 (The Mathworks, UK) using the in-built PDE solver (PDEPE). Code is provided by the authors on request.

Calculation of the change of tumour proliferation characteristics for increasing microvessel density

For model calculations in Fig 3, a heterogeneous vessel distribution as in Fig 3C was used. AVE size distributions were then calculated using the virtual tissue method as described above using the IVD as input. The observed experimental decrease of the microvessel distance between day 8 and day 18 by 27% was reflected by an increase of IVD by 37% due to the inverse relationship between both (Δ IVD ~ Δ 1/MVD; 100% / 137% = 0.73, i.e. 27 % decrease). IVD values were hence chosen as 64 µm to 85 µm for day 8 and day 18, respectively, to be centred around the experimental value of 75 µm [27].

Xenograft model

Xenograft models were established by subcutaneous injection of 2.5 x 10^6 HCT116-luc2 cells into the flank of Balb/c nude mice (Charles River Laboratories, UK). Tumours were harvested at days 8 (n = 2) and 18 (n = 2) and fixed in 10 % buffered formalin for 24 hours before being processed and paraffin embedded.

Histologic Examination and Immunohistochemistry

Paraffin-embedded, formalin-fixed tissue sections from mouse HCT116-luc2 subcutaneous tumours were stained with Hematoxylin and Eosin (H & E) and anti-luciferase stained in order to access percentage of tumour core necrosis. Anti-KI67 and anti-PECAM1/CD31 staining procedures were carried out to determine tumour cell proliferation and microvessel density respectively. In brief, tumour sections were deparaffinized with xylene and rehydrated according to standard histologic procedures. For epitope retrieval, sections were boiled for 20 minutes in 10 mM citrate buffer, pH 6.0. Sections were rinsed in Tris buffered saline (TBS)-

Tween and blocked in 5 % serum in TBS for 1 hour followed by incubation at room temperature for 1 hour with the following primary antibodies: rabbit anti-Ki-67 (Millipore, Billerica, MA), dilution 1:100; goat anti-luciferase polyclonal antibody (pAb) (Promega, Fitchburg, WI), dilution 1:50; and goat anti-PECAM-1 (M-20) (Santa Cruz Biotechnology, Inc., Dallas, TX), dilution 1:100 in TBS containing 1% serum. Biotinylated goat anti-rabbit or horse anti-goat secondary antibodies (Vector Laboratories, Burlingame, CA), dilution 1:200 in TBS/ 1 % serum, were applied for 1 hour at room temperature followed by ABC complex (Vectastain ABC kit, Vector Laboratories) incubation for 30 minutes. Positive signal was developed with diaminobenzidine (DAKO, Glostrup, Denmark) according to the manufacturer's instructions. Sections were counterstained with hematoxylin to visualize nuclei. TUNEL staining was performed according to manufacturer's recommendations using ApoptoTag Peroxidase *In Situ* Apoptosis Detection Kit (Millipore, Billerica, MA). For assessment of proliferation indices (percentage of KI-67-positive cells), fractions of labelled tumour cells were assessed in 10 microscopic high-power fields per section using x40 magnification and ImageJ software (National Institutes of Health, Bethesda, MD). While the rabbit anti-KI67 antibody implemented cross-reacts with human and mouse tissue, histopathological analysis confirmed that the tumour rim area (outside the necrotic core and the adipose tissue) used for KI67 analysis in Fig 7 were almost exclusively (>95%) populated with tumour cells at both day 8 and day 18, and cells with a morphology consistent with infiltrating cells are not discernible.

Microvessel density based on criteria previously described [54] was assessed.

To quantify percentage of tumour core necrosis, whole slides were first scanned on a Leica microsystems whole slide imaging platform (Leica Microsystems, Wetzlar, Germany) and then area of tumour core necrosis versus whole tumour area was calculated using ImageJ software (National Institutes of Health, Bethesda, MD). Alternatively, representative images of stained

tissue slides were captured using a Nikon 2000s epi fluorescence microscope with a Hamamatsu Orca 285 camera (Micron-Optical, Wexford, Ireland).

Data Analysis

Data are presented as the mean ± standard error of the mean (SEM). Two-group comparison was made using unpaired t-test or Mann Whitney test (PRISM GraphPad Software In.c., La Jolla, CA). Significance was accepted at $p < 0.05$.

Acknowledgements

The project has received funding from the European Union Marie Curie action project Oxysense PIAP-GA-2009-230641 (JHMP), the Science Foundation Ireland Grant 08/IN.1/B1949 (JHMP and HJH), the European Union's Seventh Framework Programme ANGIOPREDICT' (www.angiopredict.com) (to ATB) under grant agreement no 278981 and the Bijzonder Onderzoeksfonds of the KU Leuven (PF/10/014) to HJH.

References:

1. Carmeliet, P. and R.K. Jain, *Principles and mechanisms of vessel normalization for cancer and other angiogenic diseases.* Nat Rev Drug Discov, 2011. **10**(6): p. 417-27.
2. Crawford, Y. and N. Ferrara, *VEGF inhibition: insights from preclinical and clinical studies.* Cell Tissue Res, 2009. **335**(1): p. 261-9.
3. Folkman, J., *Tumor angiogenesis: therapeutic implications.* N Engl J Med, 1971. **285**(21): p. 1182-6.
4. Harting, C., et al., *Single-cell-based computer simulation of the oxygen-dependent tumour response to irradiation.* Phys Med Biol, 2007. **52**(16): p. 4775-89.
5. Owen, M.R., et al., *Angiogenesis and vascular remodelling in normal and cancerous tissues.* J Math Biol, 2009. **58**(4-5): p. 689-721.
6. Mattern, J., R. Koomagi, and M. Volm, *Association of vascular endothelial growth factor expression with intratumoral microvessel density and tumour cell proliferation in human epidermoid lung carcinoma.* Br J Cancer, 1996. **73**(7): p. 931-4.
7. Vartanian, R.K. and N. Weidner, *Correlation of intratumoral endothelial cell proliferation with microvessel density (tumor angiogenesis) and tumor cell proliferation in breast carcinoma.* Am J Pathol, 1994. **144**(6): p. 1188-94.
8. Hlatky, L., P. Hahnfeldt, and J. Folkman, *Clinical application of antiangiogenic therapy: microvessel density, what it does and doesn't tell us.* J Natl Cancer Inst, 2002. **94**(12): p. 883-93.
9. Lee, J.S., et al., *Correlation between angiogenesis, apoptosis and cell proliferation in invasive ductal carcinoma of the breast and their relation to tumor behavior.* Anal Quant Cytol Histol, 2001. **23**(2): p. 161-8.
10. Drasdo, D. and S. Hohme, *A single-cell-based model of tumor growth in vitro: monolayers and spheroids.* Phys Biol, 2005. **2**(3): p. 133-47.
11. Gatenby, R.A. and E.T. Gawlinski, *A reaction-diffusion model of cancer invasion.* Cancer Research, 1996. **56**(24): p. 5745-5753.
12. Gatenby, R.A., et al., *Acid-mediated tumor invasion: a multidisciplinary study.* Cancer Research, 2006. **66**(10): p. 5216-5223.
13. Welter, M., K. Bartha, and H. Rieger, *Vascular remodelling of an arterio-venous blood vessel network during solid tumour growth.* Journal of Theoretical Biology, 2009. **259**(3): p. 405-422.
14. Welter, M. and H. Rieger, *Physical determinants of vascular network remodeling during tumor growth.* Eur Phys J E Soft Matter, 2010. **33**(2): p. 149-63.
15. Huber, H.J., et al., *Mathematical modelling of the mitochondrial apoptosis pathway.* Biochim Biophys Acta, 2011. **1813**(4): p. 608-15.
16. Huber, H.J., R.G. McKiernan, and J.H. Prehn, *Harnessing system models of cell death signalling for cytotoxic chemotherapy: towards personalised medicine approaches?* J Mol Med (Berl), 2014. **92**(3): p. 227-37.
17. Chen, D., Y. Jiao, and S. Torquato, *A cellular automaton model for tumor dormancy: emergence of a proliferative switch.* PLoS One, 2014. **9**(10): p. e109934.
18. Jiao, Y. and S. Torquato, *Emergent behaviors from a cellular automaton model for invasive tumor growth in heterogeneous microenvironments.* PLoS Comput Biol, 2011. **7**(12): p. e1002314.
19. Patel, A.A., et al., *A cellular automaton model of early tumor growth and invasion.* J Theor Biol, 2001. **213**(3): p. 315-31.

20. Bertuzzi, A., et al., *Necrotic core in EMT6/Ro tumour spheroids: Is it caused by an ATP deficit?* J Theor Biol, 2010. **262**(1): p. 142-50.
21. Casciari, J.J., S.V. Sotirchos, and R.M. Sutherland, *MATHEMATICAL-MODELING OF MICROENVIRONMENT AND GROWTH IN EMT6/RO MULTICELLULAR TUMOR SPHEROIDS.* Cell Proliferation, 1992. **25**(1): p. 1-22.
22. Ahmed, N.Y., A.T. Ismail, and T.S. Kareem, *A clinicopathologic study of Ki-67 proliferation index in colorectal carcinoma.* Saudi Med J, 2012. **33**(8): p. 841-5.
23. Oshima, C.T., K. Iriya, and N.M. Forones, *Ki-67 as a prognostic marker in colorectal cancer but not in gastric cancer.* Neoplasma, 2005. **52**(5): p. 420-4.
24. Weber, J.C., et al., *Is a proliferation index of cancer cells a reliable prognostic factor after hepatectomy in patients with colorectal liver metastases?* Am J Surg, 2001. **182**(1): p. 81-8.
25. Pries, A.R., et al., *Structural adaptation and heterogeneity of normal and tumor microvascular networks.* PLoS Comput Biol, 2009. **5**(5): p. e1000394.
26. Travasso, R.D., et al., *Tumor angiogenesis and vascular patterning: a mathematical model.* PLoS One, 2011. **6**(5): p. e19989.
27. Konerding, M.A., E. Fait, and A. Gaumann, *3D microvascular architecture of pre-cancerous lesions and invasive carcinomas of the colon.* British Journal of Cancer, 2001. **84**(10): p. 1354-1362.
28. Bakker, J., et al., *Serial blood lactate levels can predict the development of multiple organ failure following septic shock.* Am J Surg, 1996. **171**(2): p. 221-6.
29. Diabetes Prevention Trial--Type 1 Diabetes Study, G., *Effects of insulin in relatives of patients with type 1 diabetes mellitus.* N Engl J Med, 2002. **346**(22): p. 1685-91.
30. Van der Schueren, B., et al., *Low cytochrome oxidase 4I1 links mitochondrial dysfunction to obesity and type 2 diabetes in humans and mice.* Int J Obes (Lond), 2015. **39**(8): p. 1254-63.
31. Jiang, Y., et al., *A multiscale model for avascular tumor growth.* Biophys J, 2005. **89**(6): p. 3884-94.
32. Jarzabek, M.A., et al., *In vivo bioluminescence imaging validation of a human biopsy-derived orthotopic mouse model of glioblastoma multiforme.* Mol Imaging, 2013. **12**(3): p. 161-72.
33. Bartha, K. and H. Rieger, *Vascular network remodeling via vessel cooption, regression and growth in tumors.* J Theor Biol, 2006. **241**(4): p. 903-18.
34. Baish, J.W., et al., *Scaling rules for diffusive drug delivery in tumor and normal tissues.* Proc Natl Acad Sci U S A, 2011. **108**(5): p. 1799-803.
35. Risser, L., et al., *From homogeneous to fractal normal and tumorous microvascular networks in the brain.* J Cereb Blood Flow Metab, 2007. **27**(2): p. 293-303.
36. Tannock, I.F., *The relation between cell proliferation and the vascular system in a transplanted mouse mammary tumour.* Br J Cancer, 1968. **22**(2): p. 258-73.
37. Goel, S., et al., *Normalization of the vasculature for treatment of cancer and other diseases.* Physiol Rev, 2011. **91**(3): p. 1071-121.
38. Jain, R.K., *Determinants of tumor blood flow: a review.* Cancer Res, 1988. **48**(10): p. 2641-58.
39. Jain, R.K., *Normalization of tumor vasculature: an emerging concept in antiangiogenic therapy.* Science, 2005. **307**(5706): p. 58-62.
40. Hemmerlein, B., et al., *Vascular endothelial growth factor expression, angiogenesis, and necrosis in renal cell carcinomas.* Virchows Arch, 2001. **439**(5): p. 645-52.

41. Hanahan, D. and R.A. Weinberg, *Hallmarks of cancer: the next generation.* Cell, 2011. **144**(5): p. 646-74.
42. Liefers, G.J., et al., *Micrometastases and survival in stage II colorectal cancer.* N Engl J Med, 1998. **339**(4): p. 223-8.
43. Choe, S.C., et al., *Model for in vivo progression of tumors based on co-evolving cell population and vasculature.* Sci Rep, 2011. **1**: p. 31.
44. Godde, R. and H. Kurz, *Structural and biophysical simulation of angiogenesis and vascular remodeling.* Developmental Dynamics, 2001. **220**(4): p. 387-401.
45. Gerlee, P. and S. Nelander, *The impact of phenotypic switching on glioblastoma growth and invasion.* PLoS Comput Biol, 2012. **8**(6): p. e1002556.
46. Frieboes, H.B., et al., *Three-dimensional multispecies nonlinear tumor growth-II: Tumor invasion and angiogenesis.* Journal of Theoretical Biology, 2010. **264**(4): p. 1254-1278.
47. Wise, S.M., et al., *Three-dimensional multispecies nonlinear tumor growth - I - Model and numerical method.* Journal of Theoretical Biology, 2008. **253**(3): p. 524-543.
48. Stieß, M., *Mechanische Verfahrenstechnik - Partikeltechnologie 1*. 2009, Berlin, Heidelberg.
49. Mahmood, M.S., S. Mahmood, and D. Dobrota, *Formulation and numerical simulations of a continuum model of avascular tumor growth.* Mathematical Biosciences, 2011. **231**(2): p. 159-171.
50. Pettet, G.J., et al., *The migration of cells in multicell tumor spheroids.* Bulletin of Mathematical Biology, 2001. **63**(2): p. 231-257.
51. Freyer, J.P. and R.M. Sutherland, *A REDUCTION IN THE INSITU RATES OF OXYGEN AND GLUCOSE CONSUMPTION OF CELLS IN EMT6/RO SPHEROIDS DURING GROWTH.* Journal of Cellular Physiology, 1985. **124**(3): p. 516-524.
52. Fick, A., *Ueber Diffusion.* Ann. Phys., 1855. **170**: p. 59–86.
53. Chandrasekhar, S., *Stochastic Problems in Physics and Astronomy.* Reviews of Modern Physics, 1943. **15**(1).
54. Leonard, E.C., J.L. Friedrich, and D.P. Basile, *VEGF-121 preserves renal microvessel structure and ameliorates secondary renal disease following acute kidney injury.* Am J Physiol Renal Physiol, 2008. **295**(6): p. F1648-57.
55. Freyer, J.P., *RATES OF OXYGEN-CONSUMPTION FOR PROLIFERATING AND QUIESCENT CELLS ISOLATED FROM MULTICELLULAR TUMOR SPHEROIDS.* Oxygen Transport to Tissue Xv, 1994. **345**: p. 335-342.

Figure Legends

Figure 1: Schematic representation of the method for decomposing vascular tissue into avascular elements (AVEs) (**A**) A vascular tumour is decomposed into different AVEs. Here four elements of different sizes are illustrated by different colours. **(B**) These elements (depicted as rectangles for convenience and colour code relating to (A), indicating different element sizes) were considered to exchange nutrients, waste and cells via diffusion. The small arrows indicate the exchange among the elements. Every AVE was assumed to be connected to an AVE of a different size with a probability proportional to their relative occurrence (**C**). This AVE size distribution is characterised by a histogram, whereby AVE's are binned according their size. The shape of the histogram is an indicator of the regularity of the vessel system. (**D**) AVE geometry was simplified via a half cylindrical shape with a vessel at the centre and with a height being equal to the diameter of the cylinder. These assumptions reduced the mathematical complexity of the PDE system.

Figure 2: Implementation of transition rates and numerical procedure (**A**) Scheme depicting the dependency of the three transition rates $\boldsymbol{K_P}$, $\boldsymbol{K_Q}$ and $\boldsymbol{K_D}$ on oxygen (c_o), glucose (c_g) and lactate (waste; c_w) concentrations at three different conditions. Cell death conditions (left panel) occur when either oxygen or glucose is below or waste is above a specific threshold value (Suffix T). Change from quiescence to proliferating cells occurs when concentrations exceed the proliferation threshold (medium panel; Suffix PT). Optimum conditions (Suffix opt) are achieved when, at the same time, oxygen and glucose are above and waste is below a specific concentration threshold (right panel). Between these thresholds, transition rates were interpolated using sine and cosine scaled to the descending and ascending quadrant to reflect the monotonous dependency of these rates on nutrients and wastes. **(B)** Transitions between proliferating (P), quiescent (Q) and dead (D) tumour cells are depicted. Above the proliferation

threshold, tumour cells proliferate at rate K_B and quiescent cells become proliferating at rate K_P. Below the proliferation threshold, proliferating cells become quiescent at rate K_Q. Below the survival threshold, quiescent cells died at rate K_D and were removed according to a removal rate K_R. **(C)** The iterative procedure to calculate the AVE exchange term is depicted. A nested procedure was used. The inner iteration was used to solve Eqs. 1-3 along with Eqs. 4-9 at a certain time step t during a time interval Δt until AVE source terms were stable. Use of the time interval Δt allowed to consider the AVE exchange terms constant with respect to time during this comparably small interval. This decoupled the Eqs. 1-3 from Eqs. 4-9 in their time dependence and facilitated the numerical solution. In the outer loop, iteration was performed over subsequent time steps to account for the time dependency of AVE exchange terms. As starting conditions for each time step, AVE exchange terms of the previous step were used. The outer integration was stopped until also convergence for P, Q and D cells was achieved. Finally, the average number of P, Q and D cells per volume for a specific vascularisation were extracted.

Figure 3: Calculated distribution of proliferating, quiescent and dead cells, and cell density over time emerging from homogenous and heterogeneous vascularisation (A-B) The principle of determining the relative abundance of AVEs with a characteristic diameter RAVE and its application to homogenous and heterogeneous vascularity is given**.** A virtual 2D tissue was assumed for homogenous (**A**) and heterogeneous (**B**) vasculature (red spots). The distance to the two nearest adjoining vessels $(\mathbf{r_1}, \mathbf{r_2})$ from randomly placed dots was calculated assigning the characteristic length $R_{AVE} = ½ \text{ abs}(\mathbf{r_1} + \mathbf{r_2})$ (see magnified graph). Volumes were calculated according Fig 1D to reflect 3D avascular elements (AVE). (**C**) Histograms for AVE distributions using a homogenous (grey bar) or heterogeneous (black bar) vasculature from the same average vessel density were given as derived from this procedure. **(D)** Calculated distribution of proliferating, quiescent and dead cells for a homogenous and heterogeneous

vasculature (left column) with the same average IVD of 75 μm from panel C. While under a homogenous vasculature (E; absolute numbers Q: $4.7 \cdot 10^8$, P: $1.6 \cdot 10^6$, D: $5.0 \cdot 10^5$), the amount of proliferating cells was negligible, a higher amount of these cells, and therefore a higher cell turnover, was predicted with a heterogeneous distribution (absolute numbers Q: $3.0 \cdot 10^8$, P: $5.1 \cdot 10^7$, D: $3.7 \cdot 10^7$. **(E, G)** relative distribution of P (black), Q (dark grey) and D cells (light grey) in each of the 10 AVEs for homogenous and heterogeneous tissue, respectively. Larger AVEs numbers depict bigger AVEs as characterised by the Radius R_{AVE} from Fig 3C. For the homogenous tissue (E), only quiescent cells were present in most of the AVEs, while only the two biggest AVEs showed some dead and proliferating cells. For the heterogeneous tissue (G), proliferating cells were most prominent in the best perfused, smallest AVE, while dead cells were prominent in larger AVEs. Notably, compensatory proliferation, whereby dead cells are replaced was noted in medium size AVEs (proliferating rate higher in AVE 5-8 than in AVE 3). **(F, H)** Volume weighted relative distribution of P, Q, D cells for the homogenous (F) and heterogeneous tissue (H) are given, giving the percentages of cells of each type and in each AVE relative to the entire tissue (100%).

Figure 4: Sensitivity analysis of the model Parameters that were not obtained from literature were subjected to a local sensitivity analysis, whereby each parameter was varied independently by 10%. Parameters are described in Table 1. The heterogeneous distribution from Fig. 3 was used (average IVD of 75 μm). (**A-B**) Values of P, Q and D cells were given relative to the tissue and absolute deviation of these relative percentages were calculate when a parameter was changed by +/- 10 % compared to the one obtained by the reference value of the parameter of Table 1. The vessel permeability θ was identified as the most influential parameter. Only parameters which changed the cell composition by more than 0.1% were shown. **(C)** Same as (AB) for the cell compositions when using a different number of AVEs.

Figure 5: Change of cell composition over different amount of vascularisation reveals a peak of proliferating and dead cells around and average IVD of 80 μm (A) Cell numbers for P (black dashed line), Q (dark grey dotted line), and D (light grey solid line) cells were given for heterogeneous tissues with different average IVDs. While the average amount of cells per tissue steadily decreased due to lack of nutrient supply, the amount of proliferating cells reached a peak at about 80 μm as the decreasing overall cell number at regimens between 50 and 80 μm allowed for quiescent cells to re-enter a proliferating state. dead cells matched that trend of proliferating cells. **(B-D)** Amount of oxygen (B) and glucose (C) supply together with lactate (waste, D) concentration over different heterogeneous tissues with given average IVD. Survival threshold, proliferation thresholds and optimal concentrations for the respective entities are given by dotted, small dashed and large dashed lines. Notably, oxygen levels cross the optimum proliferation threshold at ~80 μm, leading to a decrease of proliferation at tissues with higher average IVD (lower vessel density). (**E**) Comparison of proliferating and dead cells for tissues with average IVDs of 64 and 85 that are around the peak of proliferating and dead cells. We observed an increase of 38% and 31%, respectively, despite a tissue with lower vessel density. The increase in the average IVD of 37% matched the decrease of microvessel distance in Fig 6B of 27% due to an inverse relation between both. (**F, G**) Volume weighted relative distribution of P, Q, D cells for a heterogeneous vessel distribution of Fig. 3C and average IVDs of 64 (F) and 85 (G) are given. The percentages of cells of each type in each AVE are given relative to the entire tissue (100%).

Figure 6: Model can predict evolution of tumour cells caused by changes in vascular density Microvessel density (MVD), proliferation index and number of apoptotic cells were detected using a HCT116-luc2 SQ tumour mouse xenograft model and harvesting tumours at day 8 and 18. **(A-C)** Representative images of PECAM1/CD31 staining are given (A-B).

Staining was analysed for two mice for each time point using 10 randomly chosen fields outside the necrotic core lead to a significant decrease ($p = 0.0059$) in MVD from Day 8 (22.4 ± 2.4) to Day 18 (16.3 ± 2.2; C). This relative decrease of 27% was considered as equal to an increase of 37% in the average IVD in our model according to their inverse relation. **(D-F)** Evolution of proliferating cells between day 8 and day 18. KI67 antibody was used for staining proliferating cells (D-E). A significant increase ($p = 0.0006$) of proliferation in day 18 tumours was observed from 19.7 ± 1.7 % (day 8) to 28.3 ± 1.6 % (day 18), as MVD decreased (F). This experimental increase in proliferating cells (44%) was matched by the model (38%). **(G-I)** Evolution of dead cells from day 8 to day 18 as MVD decreases. TUNEL-staining of representative fields outside the necrotic core (G-H) indicated non-significant ($p = 0.098$) increase in number of apoptotic cells (used to compare with the dead cells from the model) from 5.8 ± 0.7 % (day 8) to 8.0 ± 0.8 (day 18). Increase in dead cells (38%) qualitatively matched model data (31%). For all staining data bars represent mean ± SEM (day 8 ($n = 10$ images per tumour, $n = 2$ animals), day 18 ($n=10$ images per tumour, $n = 2$ animals), quantifications from 10 randomly chosen field of views per section outside the necrotic core for each of the two mice sacrificed at the indicated dates, scale bar = 25 μm, * - $p < 0.05$, ns – non-significant, Mann-Whitney test

Supplementary Figure 1: Transition rates and cellular distributions

(**A-B**) Transition rates between P and Q in dependence on glucose and oxygen concentration relative to their optimal values ($c_{g\ opt}$ and $c_{o\ opt}$). **(C, D)** Spatial distribution of the different cell types for the homogenous and the heterogeneous distribution were re-generated by randomly assigning the AVEs to spatial locations for illustration purposes. Dots were coloured according to the probability of P, Q, or D cells in the particular AVE. Islands of cell death in the heterogeneous vessel distribution in (D) indicate high accumulation of dead cells arising from

large AVE elements that were insufficiently supplied by nutrients or affected by high waste accumulation.

Supplementary Figure 2: Extended sensitivity analysis

Each parameter was varied independently by +/-10%. Parameters are described in Table 1. The heterogeneous distribution from Fig. 3 was used (average IVD of 75 μm). (**A-B**) Absolute changes of P, Q and D cells were calculated when a parameter was changed by +/- 10 % and given relative to the cell composition obtained when using the reference value of the parameter of Table 1. The vessel permeability θ was identified as the most influential parameter (**C**) Same as (AB) for the cell compositions when using different numbers of AVEs.

Supplementary Figure 3: Stability of our method (Fig. 2C) to initial conditions Different initial conditions were used for the heterogeneous tissue with AVE=75 of Fig 3 from the main text and temporal evolvement of P, Q and D cells and the total cell density was calculated (A-D, respectively). Convergence was achieved at about 100 time steps. For the interpretation of time steps, please refer to the methods section.

Tables

Table 1: List of constants used in the model Rates for nutrient consumption, waste production, diffusion of cells and nutrients, and concentration thresholds for nutrients and waste for determining cell proliferation and death, were given along with their references.

Constant	Description	Value/ Source
f_{o_P} [mol /(h . cell)]	Oxygen consumption of proliferating cells	$3 \cdot 10^{-13}$ [51]
f_{g_P} [mol /(h . cell)]	Glucose consumption of proliferating cells	$= {}^{162}/_{108} \cdot \mathrm{f_{o_P}}$ [31, 55]
f_{w_P} [mol /(h . cell)]	Waste production of proliferating cells	$= {}^{240}/_{108} \cdot \mathrm{f_{o_P}}$ [31, 55]
f_{o_Q} [mol /(h . cell)]	Oxygen consumption of quiescent cells	$= {}^{50}/_{108} \cdot \mathrm{f_{o_P}}$ [31, 55]
f_{g_Q} [mol /(h . cell)]	Glucose consumption of quiescent cells	$= {}^{80}/_{50} \cdot \mathrm{f_{o_Q}}$ [31, 55]
f_{w_Q} [mol /(h . cell)]	Waste production of quiescent cells	$= {}^{110}/_{50} \cdot \mathrm{f_{o_Q}}$ [31, 55]
$f_{o_N}, f_{g_N}, f_{w_N}$	Metabolic rates of dead cells	0 (assumed)
D_p[$\mathrm{cm^2/h}$]	Empty space P cell diffusion constant	$9.72 \cdot 10^{-7}$ [31]
D_q[$\mathrm{cm^2/h}$]	Empty space Q cell diffusion constant	$0.9 \cdot D_p$ (assumed)
D_n[$\mathrm{cm^2/h}$]	Empty space N cell diffusion constant	0 (assumed)
D_o[$\mathrm{cm^2/h}$]	oxygen diffusion constant	$5.94 \cdot 10^{-2}$ [31]
D_g[$\mathrm{cm^2/h}$]	glucose diffusion constant	$1.52 \cdot 10^{-3}$ [31]
D_w[$\mathrm{cm^2/h}$]	waste diffusion constant	$2.12 \cdot 10^{-3}$ [31]
c_{o_T}[mol /$\mathrm{cm^3}$]	Survival threshold for oxygen	$0.04 \cdot 10^{-6}$ [31]
$c_{o_{opt}}$[mol /$\mathrm{cm^3}$]	optimal oxygen concentration	$0.28 \cdot 10^{-6}$ [31]
$c_{o_{PT}}$[mol /$\mathrm{cm^3}$]	Proliferation threshold for oxygen	$c_{g_{PT}} + \frac{(c_{g_{opt}} - c_{g_T})}{3.5}$ (assumed)
c_{g_T}[mM]	Survival threshold for glucose	$0.06 \cdot 10^{-6}$ [31]
$c_{g_{opt}}$[mM]	optimal glucose concentration	$5.5 \cdot 10^{-6}$ [31]
$c_{g_{PT}}$[mM]	Proliferation threshold for waste	$c_{w_T} - \frac{c_{w_T}}{3.5}$ (assumed)
c_{w_T}[mM]	Survival threshold for waste	$8 \cdot 10^{-6}$ [31]
$c_{w_{opt}}$[mM]	optimal glucose waste	0 [31]
$c_{w_{PT}}$[mM]	Proliferation threshold for glucose	$c_{w_T} - \frac{c_{w_T}}{3.5}$ (assumed)
ϑ [$\mathrm{cm^2/h}$]	Vessel permeability	18.5*D_o (assumed)

K_q [1/h]	Maximal transition rate between Q and P cells	$\frac{\log(2)}{4}$ (assumed)
K_p [1/h]	Maximal transition rate between P and Q cells (if survival thresholds are not reached)	$\frac{\log(2)}{4}$ (assumed)
K_B [1/h]	Rate of cell birth	0.047 [49]
K_r[1/h]	Maximal removal rate of dead cells	$\frac{\log(2)}{1.5}$ (assumed)

Table 2: Limiting conditions for cell transition rates: Transition rates for the amount of quiescent cells becoming proliferating K_P, the amount of proliferating cells becoming quiescent K_Q and for the number of quiescent cells dead K_D were given when different nutrient and waste concentrations converged against specific thresholds. The conditions are explained using c_o as example.

Situation	**Condition**	**Transition Parameter**	**Remark**
Approach optimum concen-tration	$c_{o\,PT} < c_o \rightarrow c_{o_{opt}}$ $c_{g\,PT} < c_g \rightarrow c_{g_{opt}}$ $c_{w\,PT} > c_w \rightarrow c_{w_{opt}}$ if $cd < 0.8 \cdot cd_{max}$	$K_Q \rightarrow 0$ $K_P \rightarrow K_p$ (= maximum value) $K_D = 0$	Under optimal conditions (glucose and oxygen above optimum concentration and waste below) no proliferating cells become quiescent, and quiescent cells become proliferating with a constant rate
Approach prolifer-ation threshold	$c_{o_{opt}} > c_o \rightarrow c_{o\,PT}$ $c_{g_{opt}} > c_g \rightarrow c_{g\,PT}$ $c_{w_{opt}} < c_w \rightarrow c_{w\,PT}$ if $cd < 0.8 \cdot cd_{max}$	$K_Q \rightarrow K_q$ $K_P \rightarrow 0$ $K_D = 0$	If conditions approach the proliferation threshold the transition rate of proliferating to quiescent cells becomes a constant
Approach survival threshold	$c_{o\,PT} > c_o \rightarrow c_{o\,T}$ $c_{g\,PT} > c_g \rightarrow c_{g\,T}$ $c_{w\,PT} < c_w \rightarrow c_{w\,T}$ if $cd < 0.8 \cdot cd_{max}$	$K_Q = K_q$ $K_P = 0$ $K_D = 0$	Above the survival threshold the cell death rate starts is still zero
Below survival threshold	$c_{o\,T} > c_o \rightarrow 0$ $c_{g\,T} > c_g \rightarrow 0$ $c_{w\,T} < c_w \rightarrow \infty$	$K_Q \rightarrow \infty$ $K_D \rightarrow \infty$ $K_P = 0$	If conditions demand cell death, all proliferating cells had to become quiescent first and all quiescent cells die immediately
Increasing cell density	$cd \rightarrow cd_{max}$	$K_P \rightarrow 0$ $K_Q \uparrow$ $D_P, D_{Q,} D_N \rightarrow 0$	Under lack of space the number of proliferating cells and cell diffusion vanishes. See Table 4 for specifics.

Table 3: Transition rates for general situation: Transition rates were given for the amount of quiescent cells becoming proliferating K_P, the amount of proliferating cells becoming quiescent K_Q and for the number of quiescent cells dead $K_{D,}$ when no concentration approaches a threshold. Rates were determined by their most restrictive factor $\widetilde{K_Q} = max[K_{Qo}, K_{Qg}, K_{Qw}]$, $\widetilde{K_P} = min[K_{Po}, K_{Pg}, K_{Pw}]$, $\widetilde{K_D} = max[K_{Do}, K_{Dg}, K_{Dw}]$ and corrected for the amount of available space according Table 4.

Limiting factor	Condition	Transition Parameter Values
Oxygen	Below optimum, but above proliferation threshold $c_{o\,PT} < \mathrm{c_o} < c_{o\,opt}$	$K_{Qo} = K_q \cdot \cos\left(\frac{\pi}{2} \cdot \frac{c_o - c_{o_{PT}}}{c_{o_{opt}} - c_{o_{PT}}}\right)^2$ $K_{Po} = K_p \cdot \sin(\frac{\pi}{2} \cdot \frac{c_o - c_{o\,PT}}{c_{o\_opt} - c_{o\,PT}})^2$ $K_{Do} = 0$
Oxygen	Below proliferation, but above survival threshold $c_{o\,T} < \mathrm{c_o} < c_{o\,PT}$	$K_{Qo} = K_q K_{Po} = 0$ $K_{Do} = 0$
Oxygen	Below survival threshold $0 < \mathrm{c_o} < c_{o\,T}$	$K_{Qo} = K_q + \left(\frac{c_{o\,T}}{c_o} - 1\right)^2$ $K_{Po} = 0$ $K_{Do} = 6 \cdot \left(\frac{c_{o\,T}}{c_o} - 1\right)^2$
Glucose	Below optimum, but above proliferation threshold $c_{g\,PT} < \mathrm{c_g} < c_{g\,opt}$	$K_{Qg} = K_q \cdot \cos\left(\frac{\pi}{2} \cdot \frac{c_g - c_{g_{PT}}}{c_{g_{opt}} - c_{g_{PT}}}\right)^2$ $K_{Pg} = K_p \cdot \sin\left(\frac{\pi}{2} \cdot \frac{c_g - c_{g_{PT}}}{c_{g_{opt}} - c_{g_{PT}}}\right)^2$ $K_{Dg} = 0$
Glucose	Below proliferation, but above survival threshold $c_{g\,T} < \mathrm{c_g} < c_{g\,PT}$	$K_{Qg} = K_q$ $K_{Pg} = 0$ $K_{Dg} = 0$
Glucose	Below survival threshold $0 < \mathrm{c_g} < c_{g\,T}$	$K_{Qg} = K_q + \left(\frac{c_{g\,T}}{c_g} - 1\right)^2$ $K_{Po} = 0$ $K_{Do} = 6 \cdot \left(\frac{c_{g\,T}}{c_g} - 1\right)^2$
Waste	Below optimum, but above proliferation threshold $c_{w\,PT} > \mathrm{c_w} > c_{w\,opt}$	$K_{Qw} = K_q \cdot \cos\left(\frac{\pi}{2} \cdot \frac{-c_w + c_{w_{PT}}}{c_{w_{opt}} - c_{w_{PT}}}\right)^2$ $K_{Pw} = K_p \cdot \sin\left(\frac{\pi}{2} \cdot \frac{-c_w + c_{w_{PT}}}{c_{w_{opt}} - c_{w_{PT}}}\right)^2$ $K_{Dw} = 0$

Waste	Below proliferation, but above survival threshold $c_{w\,T} > \mathrm{c_w} > c_{w\,PT}$	$K_{Qw} = K_q$ $K_{Pw} = 0$ $K_{Dw} = 0$
Waste	Below survival threshold $0 > \mathrm{c_w} > c_{w\,T}$	$K_{Qw} = K_q + \left(\frac{\mathrm{c_w}}{c_{w\,T}} - 1\right)^2$ $K_{Pw} = 0$ $K_{Dw} = 6 \cdot \left(\frac{\mathrm{c_w}}{c_{w\,T}} - 1\right)^2$

Table 4: Correction of transition rates in dependence on available space Transition rates of Equation 4 and Table 3 were corrected for the amount of cell density (*cd*). Free space was assumed whenever the total concentration of cells was below $b_1 = 4.0 \cdot 10^8$ [cells/cm^3], while full space was assumed was assumed whenever the total cell density exceeded $b_2 = 4.5 \cdot 10^8$ [cells/cm^3].

$cd < b_1$	$K_P = \widetilde{K_P}$
$b_1 < cd < cd_{max}$	$K_P = \widetilde{K_P} \cdot \cos\left(\frac{\pi}{2} \cdot \frac{cd - b_1}{cd_{max}}\right)^2$
$cd < b_2$	$K_Q = \widetilde{K_Q}$
$cd > b_2$	$K_Q = \widetilde{K_Q} \cdot 100 \cdot \left(\frac{b_2 - cd}{cd_{max}}\right)^2$

Table 5: Boundary conditions for nutrient distributions: Homogenous boundary conditions were assumed to mimic optimum oxygen and glucose supply as well as maximum waste disposal for the AVE at the vessel location ($r = r_{vessel}$, i.e. at the vessel surface). Migration of cells between the vessel and the tumour were disregarded. Likewise, no flow of cells and nutrients waste was assumed. However, source term correction for cells and nutrients was considered as described in the text.

Boundary condition at vessel		**Boundary condition at surface**	
$\nabla c_{o\,(r=r_{vessel})} = \frac{\vartheta}{D_o} \cdot \left(c_{o_{vessel}} - c_{o(r=r_{vessel})}\right)$	$\nabla P_{(r=r_{vessel})} = 0$	$\nabla c_{o\,(r=R)} = 0$	$\nabla P_{(r=R)} = 0$
$\nabla c_{g\,(r=r_{vessel})} = \frac{\vartheta}{D_g} \cdot \left(c_{g_{vessel}} - c_{g(r=r_{vessel})}\right)$	$\nabla Q_{(r=r_{vessel})} = 0$	$\nabla c_{g\,(r=R)} = 0$	$\nabla Q_{(r=R)} = 0$

$\nabla c_{w(r=r_{vessel})} = \frac{\vartheta}{D_w} \cdot \left(c_{w_{vessel}} - c_{w(r=r_{vessel})}\right)$	$\nabla D_{(r=r_{vessel})} = 0$	$\nabla c_{p_{(r=R)}} = 0$	$\nabla D_{(r=R)} = 0$

1

2

1 **Figure 1**

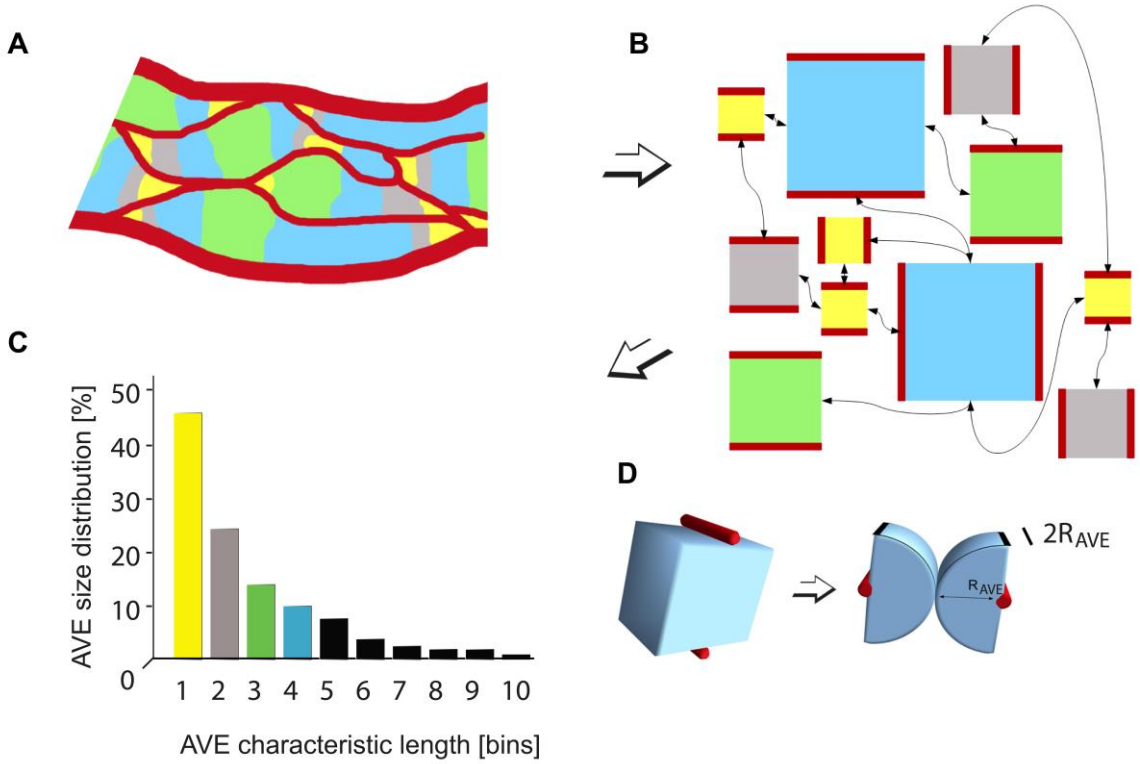
A
B
C
D
AVE size distribution [%]
0
10
20
30
40
50
1 2 3 4 5 6 7 8 9 10
AVE characteristic length [bins]
2R_AVE
R_AVE

2

3

1 **Figure 2**

2

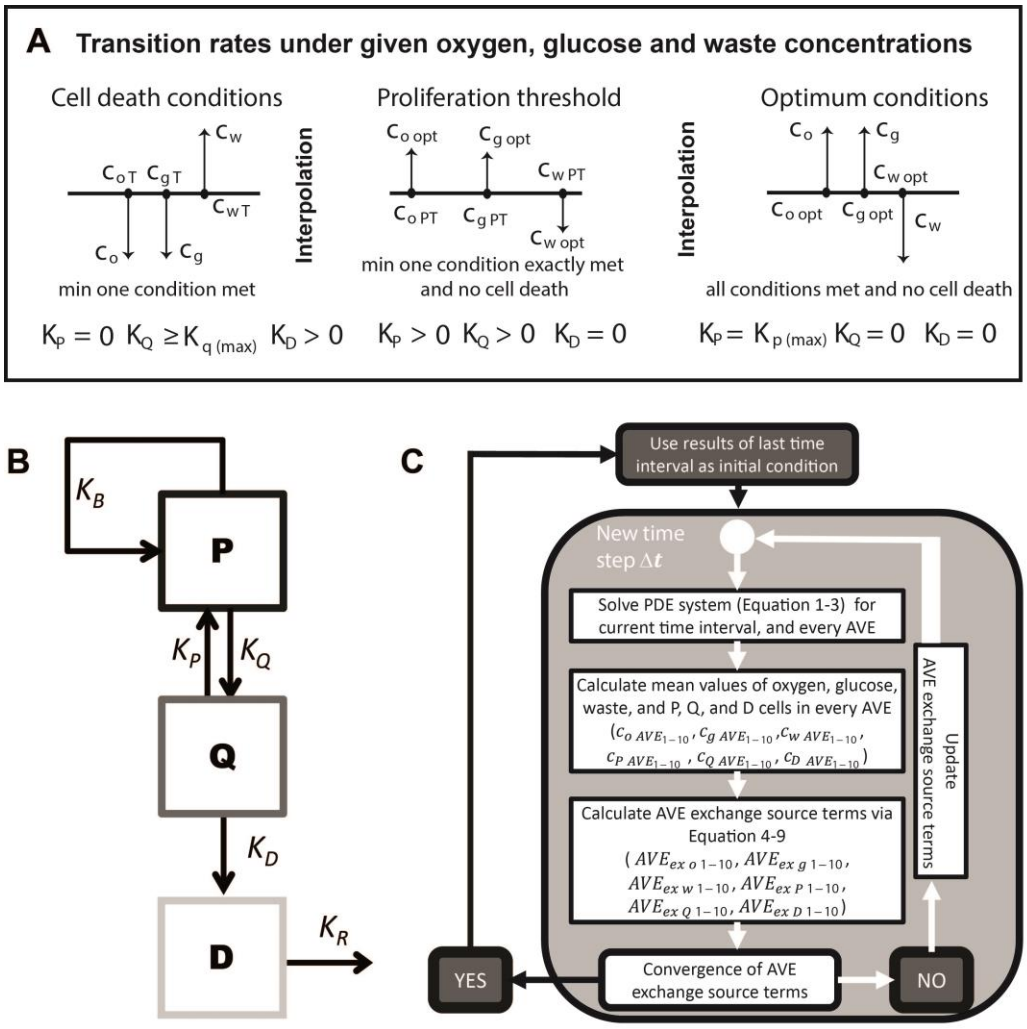

3

4

Figure 3

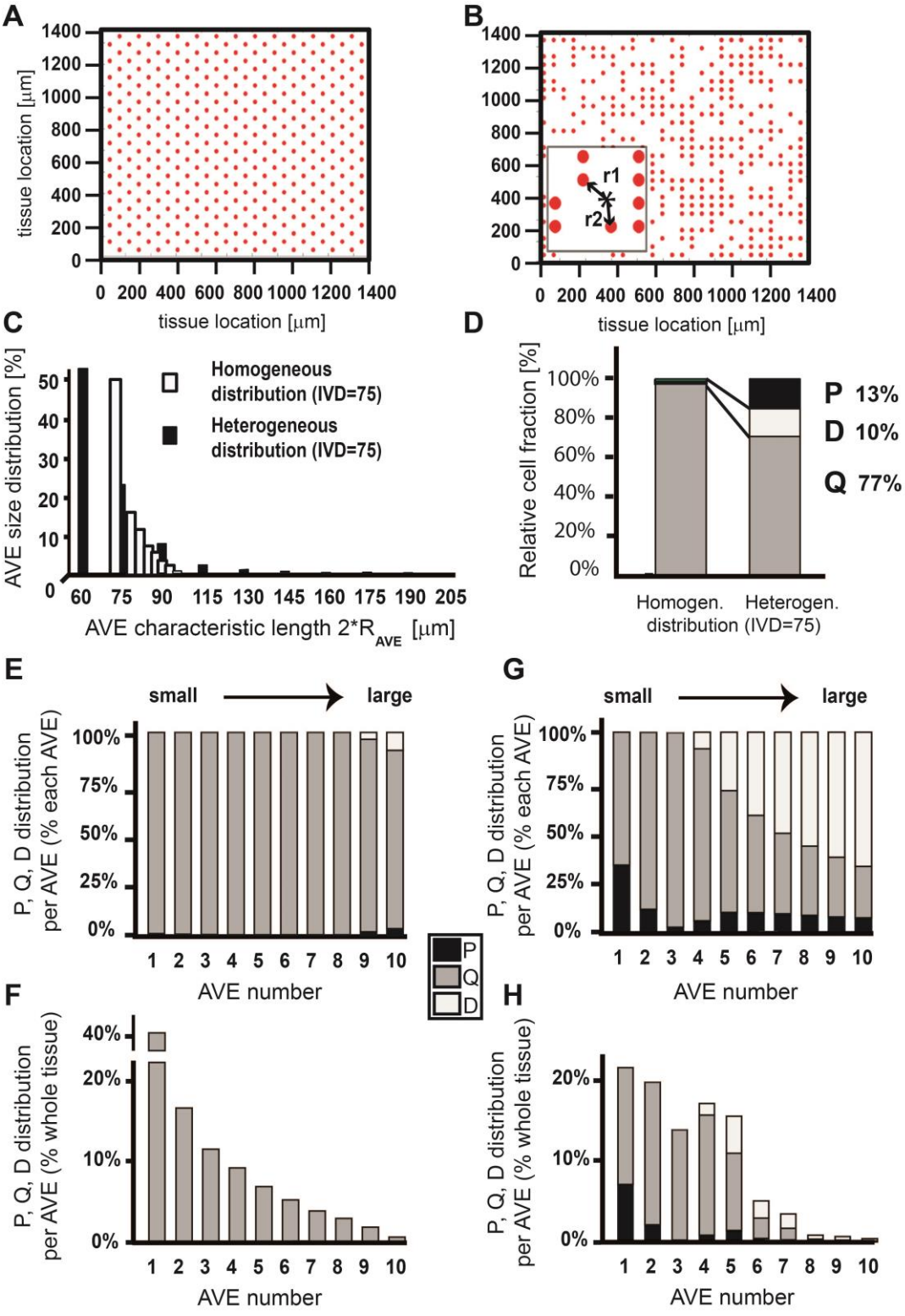
A
tissue location [μm]
tissue location [μm]
B
r1
r2
tissue location [μm]
C
AVE size distribution [%]
Homogeneous distribution (IVD=75)
Heterogeneous distribution (IVD=75)
AVE characteristic length 2*R_AVE [μm]
D
Relative cell fraction [%]
P 13%
D 10%
Q 77%
Homogen. distribution (IVD=75)
Heterogen.
E
small
large
P, Q, D distribution per AVE (% each AVE)
AVE number
G
small
large
P, Q, D distribution per AVE (% each AVE)
AVE number
P
Q
D
F
P, Q, D distribution per AVE (% whole tissue)
AVE number
H
P, Q, D distribution per AVE (% whole tissue)
AVE number

Figure 4

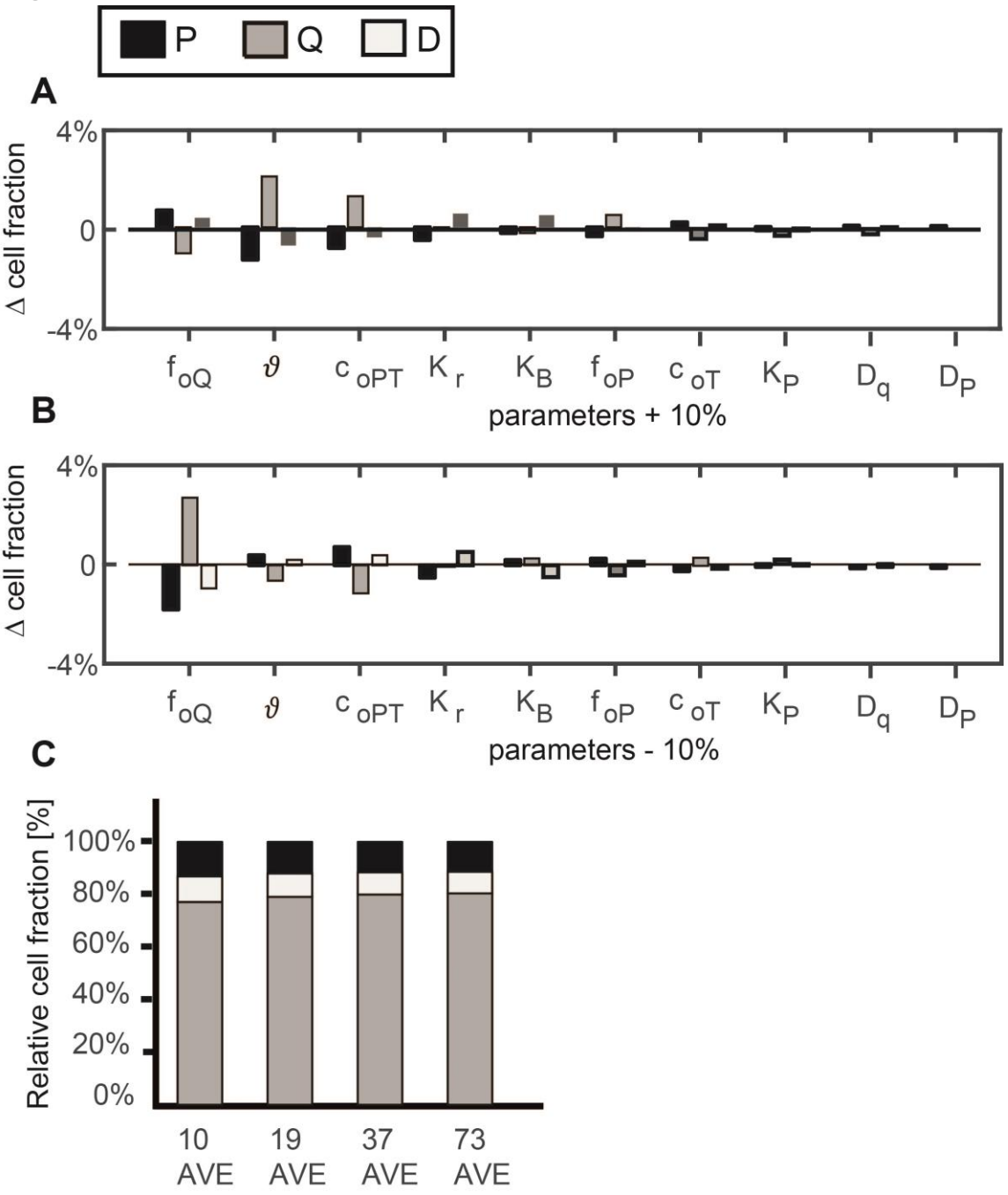
P
Q
D
A
4%
0
-4%
Δ cell fraction
f oQ
ϑ
c oPT
K r
K B
f oP
c oT
K P
D q
D P
parameters + 10%
B
4%
0
-4%
Δ cell fraction
f oQ
ϑ
c oPT
K r
K B
f oP
c oT
K P
D q
D P
parameters - 10%
C
Relative cell fraction [%]
100%
80%
60%
40%
20%
0%
10 AVE
19 AVE
37 AVE
73 AVE

1 **Figure 5**

2

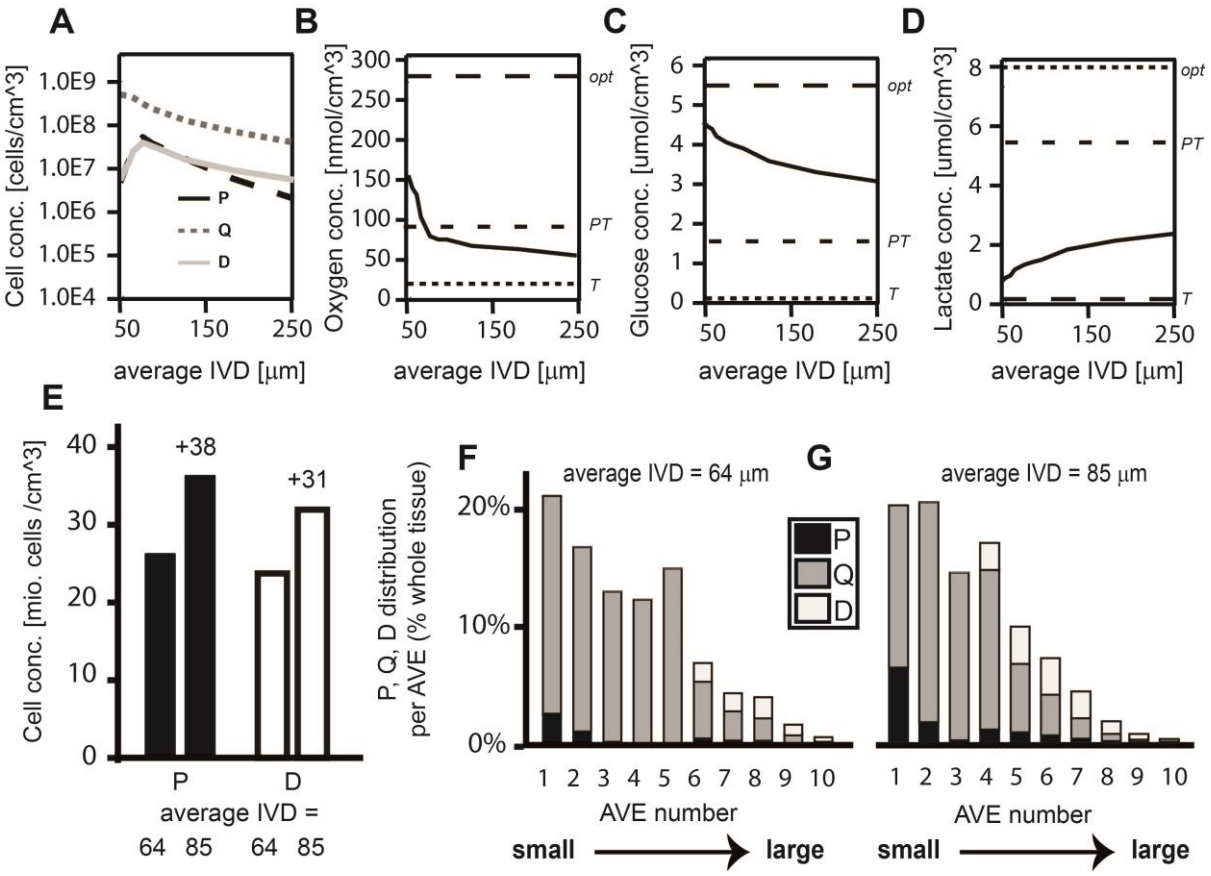

3

4

5

1 **Figure 6**

2

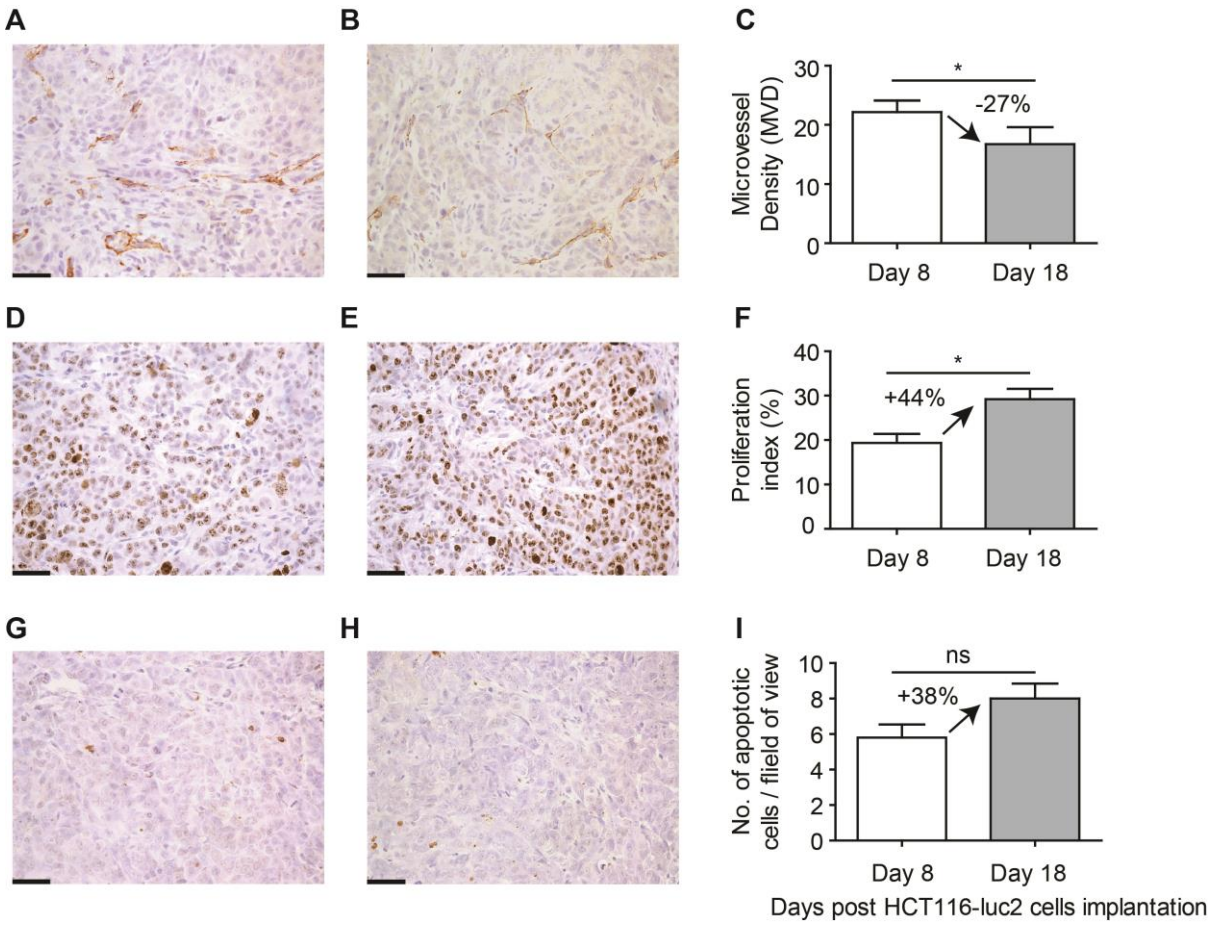
A
B
C
Microvessel Density (MVD)
30
20
10
0
*
-27%
Day 8
Day 18
D
E
F
Proliferation index (%)
40
30
20
10
0
*
+44%
Day 8
Day 18
G
H
I
No. of apoptotic cells / field of view
10
8
6
4
2
0
ns
+38%
Day 8
Day 18
Days post HCT116-luc2 cells implantation

3